

TWO BRIGHT SUBMILLIMETER GALAXIES IN A $z = 4.05$ PROTOCLUSTER IN GOODS-NORTH, AND ACCURATE RADIO-INFRARED PHOTOMETRIC REDSHIFTS

E. DADDI¹, H. DANNERBAUER², D. STERN³, M. DICKINSON⁴, G. MORRISON^{5,6}, D. ELBAZ¹, M. GIAVALISCO⁷, C. MANCINI^{1,8},
 A. POPE⁴, AND H. SPINRAD⁹

¹ CEA, Laboratoire AIM-CNRS-Université Paris Diderot, Irfu/SAP, Orme des Merisiers, F-91191 Gif-sur-Yvette, France; edaddi@cea.fr

² Max-Planck-Institut für Astronomie, Königstuhl 17, D-69117 Heidelberg, Germany

³ Jet Propulsion Laboratory, California Institute of Technology, Pasadena, CA 91109, USA

⁴ National Optical Astronomy Observatory, 950 N. Cherry Avenue, Tucson, AZ 85719, USA

⁵ Institute for Astronomy, University of Hawaii, Honolulu, HI 96822, USA

⁶ Canada–France–Hawaii Telescope, Kamuela, HI 96743, USA

⁷ University of Massachusetts, Department of Astronomy, Amherst, MA 01003, USA

⁸ Dipartimento di Astronomia, Università di Firenze, Largo E. Fermi 5, 50100 Firenze, Italy

⁹ Department of Astronomy, University of California at Berkeley, Mail Code 3411, Berkeley, CA 94720, USA

Received 2008 June 16; accepted 2008 December 30; published 2009 March 25

ABSTRACT

We present the serendipitous discovery of molecular gas CO emission lines with the IRAM Plateau de Bure interferometer coincident with two luminous submillimeter galaxies (SMGs) in the Great Observatories Origins Deep Survey North (GOODS-N) field. The identification of the millimeter emission lines as CO[4–3] at $z = 4.05$ is based on the optical and near-IR photometric redshifts, radio-infrared photometric redshifts, and Keck+DEIMOS optical spectroscopy. These two galaxies include the brightest submillimeter source in the field (GN20; $S_{850\mu\text{m}} = 20.3$ mJy, $z_{\text{CO}} = 4.055 \pm 0.001$) and its companion (GN20.2; $S_{850\mu\text{m}} = 9.9$ mJy, $z_{\text{CO}} = 4.051 \pm 0.003$). These are among the most distant submillimeter-selected galaxies reliably identified through CO emission and also some of the most luminous known. GN20.2 has a possible additional counterpart and a luminous active galactic nucleus inside its primary counterpart revealed in the radio. Continuum emission of 0.3 mJy at 3.3 mm (0.65 mm in the rest frame) is detected at 5σ for GN20, the first dust continuum detection in an SMG at such long wavelength, unveiling a spectral energy distribution that is similar to local ultra luminous IR galaxies. In terms of CO to bolometric luminosities, stellar mass, and star formation rates (SFRs), these newly discovered $z > 4$ SMGs are similar to $z \sim 2$ – 3 SMGs studied to date. These $z \sim 4$ SMGs have much higher specific star formation rates than those of typical B -band dropout Lyman break galaxies at the same redshift. The stellar mass–SFR correlation for normal galaxies does not seem to evolve much further, between $z \sim 2$ and $z \sim 4$. A significant $z = 4.05$ spectroscopic redshift spike is observed in GOODS-N, and a strong spatial overdensity of B -band dropouts and IRAC selected $z > 3.5$ galaxies appears to be centered on the GN20 and GN20.2 galaxies. This suggests a protocluster structure with total mass $\sim 10^{14} M_{\odot}$. Using photometry at mid-IR (24 μm), submillimeter (850 μm), and radio (20 cm) wavelengths, we show that reliable photometric redshifts ($\Delta z/(1+z) \sim 0.1$) can be derived for SMGs over $1 \lesssim z \lesssim 4$. This new photometric redshift technique has been used to provide a first estimate of the space density of $3.5 < z < 6$ hyper-luminous starburst galaxies, and to show that they both contribute substantially to the SFR density at early epochs and that they can account for the presence of old galaxies at $z \sim 2$ – 3 . Many of these high-redshift starbursts will be within reach of *Herschel*. We find that the criterion $S_{1.4\text{GHz}} \gtrsim S_{24\mu\text{m}}$, coupled to optical, near-IR and mid-IR photometry, can be used to select $z > 3.5$ starbursts, regardless of their submillimeter/millimeter emission.

Key words: cosmology: observations – galaxies: formation – galaxies: high-redshift – galaxies: starburst – infrared: galaxies – submillimeter

Online-only material: color figures

1. INTRODUCTION

Submillimeter and millimeter observations of galaxies are subject to strong negative K -corrections over a very broad range of redshifts, and can reach nearly constant bolometric luminosity limits (for a given flux density limit) at $1 < z < 7$ (Blain et al. 1993). This provides a powerful method for detecting and studying starburst galaxies in the distant universe. Efforts to identify counterparts of bright ($S_{850\mu\text{m}} > 5$ mJy) submillimeter-selected galaxies (see Blain et al. 2002 for a review) based on radio detections have recently suggested that the typical redshift of these sources is $z \sim 2$ (Chapman et al. 2003, 2005), with few objects at $z \sim 3$ and virtually none at $z > 4$. This result suggests a very strong decline in the space density of the

most luminous and rapidly star-forming galaxies in the distant universe.

Submillimeter galaxies (SMGs) are outliers in the stellar mass–star formation rate (SFR) relation in the $z \sim 2$ universe (Daddi et al. 2007a; Takagi et al. 2008), have gas kinematic signatures suggesting ongoing mergers (Tacconi et al. 2006, 2008), have very compact sizes reminiscent of massive, evolved galaxies at $z \sim 1.5$ – 3 (Daddi et al. 2005a; Trujillo et al. 2006; Zirm et al. 2007; Tacconi et al. 2006, 2008; Cimatti et al. 2008) and have high star formation efficiencies compared to typical galaxies of similar mass ($M \sim 10^{10}$ – $10^{11} M_{\odot}$; Daddi et al. 2008; see also Bouche et al. 2007). Their space density evolution is a crucial issue for understanding the formation of massive galaxies, as the SMGs are thought to represent massive galaxy mergers which will rapidly evolve into passive systems (Daddi

et al. 2007a, 2007b; Tacconi et al. 2008; Cimatti et al. 2008). Therefore, searching for the very high redshift tail of SMGs holds clues into understanding early-type galaxy formation and characterizing the distribution of their formation redshifts, both crucial issues for galaxy formation models in a Λ CDM universe.

The strong decline of SMG counts at redshifts higher than $z \sim 2$ might signal that $z \sim 2$ is indeed the main formation epoch of massive early-type galaxy systems (Daddi et al. 2004a, 2004b), but it can be affected by selection biases, primarily the requirement of a detection in the radio, which suffers from positive K -correction. On the other hand, the existence of a population of passive systems at $z \sim 1.5$ – 2.5 (Spinrad et al. 1997; Cimatti et al. 2004; McCarthy et al. 2004; Daddi et al. 2005a; Saracco et al. 2005; Kriek et al. 2008) with large masses $((0.5\text{--}5) \times 10^{11} M_{\odot})$, a space density of the order of 10^{-4} Mpc^{-3} ($\sim 10\%$ – 30% of the correspondent one at $z = 0$; Daddi et al. 2005a; Labbé et al. 2005; Kong et al. 2006), and estimated formation redshifts for their stars of $z \gtrsim 3$ or even much higher (Daddi et al. 2005a; Labbé et al. 2005; Maraston et al. 2006; Longhetti et al. 2007; Cimatti et al. 2008) seems to require in turn the existence of a substantial population of vigorous starburst galaxies at $z > 3$ – 4 , which should be detectable from their strong far-infrared (FIR) emission. For example, if this population of $z \sim 1.5$ – 3 early-type galaxies were mainly formed during 100 Myr long bursts within $3 < z < 6$, one would expect to find $\sim 10^{-5} \text{ Mpc}^{-3}$ galaxies with $\text{SFR} \gtrsim 1000 M_{\odot} \text{ yr}^{-1}$ in the same redshift range, which would be detectable as SMGs and with a sky density of $\approx 200 \text{ deg}^{-2}$.

Evidence has been mounting in the past years that such objects actually exist. For example, a well known case is that of HDF850.1 (Dunlop et al. 2004), an SMG in the Hubble Deep Field that is thought to be at very high redshift, lying behind a bright foreground galaxy. In addition, although largely lacking spectroscopic identifications, the survey of Dannerbauer et al. (2002, 2004) presented evidence that a high fraction of sources selected with the 1.2 mm bolometer MAMBO at the IRAM 30 m telescope (Kreysa et al. 1998) are at high redshifts, given their very faint K -band and radio detections or upper limits. Similarly, Younger et al. (2007) recently reported on seven sources selected with the AzTEC camera at 1.1 mm (Wilson et al. 2008) with flux densities above 5 mJy in the COSMOS field (Scoville et al. 2007), of which five (70%) are found to be very faint at optical and radio wavelengths, suggesting redshifts $z \gtrsim 3$ – 4 . More recently, Wang et al. (2007, 2009) and Dannerbauer et al. (2008) presented high-resolution submillimeter/millimeter imaging of a bright SMG called GN10 from Great Observatories Origins Deep Survey North (GOODS-N) field¹⁰ suggesting that this source is at a much higher redshift than thought before, probably $3.5 < z < 6$. Follow-up surveys of high-redshift radio galaxies also resulted in submillimeter detections (Archibald et al. 2001; Greve et al. 2007). Knudsen et al. (2008) proposed a $z = 4.048$ identification for SMM J16359+66130. However, this source lacks both radio and CO identifications, and to our knowledge the result was never published in a refereed journal. Recently, Capak et al. (2008) also suggest a $z = 4.547$ identification for an SMG discovered with AzTEC and IRAM in the COSMOS field. This high-redshift galaxy is $\gtrsim 1''$ away from the radio and IRAC positions. Offsets of up to $\sim 1''$ are indeed sometimes found for SMG counterparts (Chapman et al. 2005). In a few such cases the identification turned out to be wrong (see e.g.,

Pope et al. 2008); however Schinnerer et al. (2009) confirmed the $z = 4.5$ redshift for this galaxy.

Most of the evidence for $z > 4$ SMGs comes from surveys in the millimeter regime. At first glance, it is not clear how to reconcile these results with much of the follow-up work that has been done on SCUBA surveys. The slight difference in selection wavelength (850 μm versus 1.1 mm) is unlikely to be sufficient to justify the diverging results. A possible explanation is the trend for brighter SMGs to be systematically at higher redshifts, as claimed by Ivison et al. (2002) and Pope et al. (2006, P06 hereafter). Difficulties in locating the counterparts within the large submillimeter/millimeter positional uncertainties, and the fact that the most distant sources could be ultra-faint or completely undetected in the optical, near-IR, mid-IR, and/or radio, imply that it is likely to obtain incorrect identifications by choosing the brightest galaxy within the error circle of the submillimeter position. Given that star formation proceeds through the consumption of the molecular gas reservoirs, the detection of CO emission is still the most secure means to measure the redshift of an SMG.

If SMGs are the progenitors of very massive early-type galaxies, signaling perhaps their last and strongest starburst before the onset of passive evolution, they should also be strongly clustered and reside in overdense regions of the universe. Blain et al. (2004) report evidence for significant excess of redshift pairs in SMG samples, suggesting significant clustering in this population. Stevens et al. (2003) find significant excess of SMGs in the close surroundings of high-redshift radio galaxy fields, evidence that SMGs might trace protocluster environments and be related to the formation of present-day cluster ellipticals. However, this result is not yet spectroscopically confirmed. More recently, Chapman et al. (2009) discuss a $z = 1.99$ concentration of five SMGs in the GOODS-N field that does not correspond to a similarly strong overdensity of UV-selected galaxies. They suggest that concentrations of SMGs might correspond to the cosmic structures with the strongest enhancement in the frequency of major mergers.

In this paper, we take advantage of Plateau de Bure Interferometer (PdBI) observations at millimeter wavelengths in the GOODS-N area that serendipitously revealed two strong emission lines, coincident with the positions of GN20, the brightest SMG in the GOODS-N field ($S_{850\mu\text{m}} = 20.3 \text{ mJy}$), and GN20.2 ($S_{850\mu\text{m}} = 9.9 \text{ mJy}$). Using multiwavelength photometric imaging data and Keck spectroscopy, we identify the lines as CO[4–3] transitions at $z = 4.055 \pm 0.001$ and $z = 4.051 \pm 0.003$. Thanks to the serendipitous detection of CO lines in the PdBI field of view, this reverses the typical SMG counterpart identification process in which a plausible optical/near-IR counterpart with a measured spectroscopic redshift is only later confirmed through CO observations. In addition, we provide spectroscopic (CO) and photometric evidence for a second plausible counterpart to GN20.2, likely at the same redshift. This concentration of SMGs appears to define a protocluster structure as traced by B -band dropout Lyman break galaxies and massive IRAC selected $z > 3.5$ galaxies. The newly measured $z > 4$ CO redshifts for SMGs have been exploited to calibrate and test the use of radio–IR photometric redshifts for the SMG population, and to obtain a new estimate of the abundance of very high redshift SMGs.

The paper is organized as follows. In Section 2, we describe the PdBI CO line detections, and determine their redshifts in Section 3. The physical properties of the sources, in terms of molecular gas, SFRs and masses, are discussed in Section 4.

¹⁰ Here and throughout this paper we adopt the “GN” nomenclature for GOODS-N SMGs taken from Pope et al. (2006).

In Section 5, we show that these objects lie at the center of a protocluster environment. We describe a method to obtain accurate photometric redshifts for SMGs in Section 6, and discuss the properties and present a new selection technique for identifying high-redshift starbursts in Section 7. Throughout the paper magnitudes are expressed in the AB scale unless stated otherwise, and a standard cosmology is adopted with Ω_Λ , $\Omega_M = 0.76$, 0.24 and $h = H_0/(100 \text{ km s}^{-1} \text{ Mpc}^{-1}) = 0.73$.

2. PdBI OBSERVATIONS

We have used the IRAM PdBI to map the CO[2–1] transition from the $z = 1.522$ galaxy BzK-21000 (J123710.60+622234.6) redshifted to about 91.4 GHz. We obtained 7.5 hr of on-source integration in D configuration (5'5 synthesized beam) during April 2007, and 6.4 hr on-source follow-up observations were obtained in January 2008 with a B configuration (1'3 synthesized beam). For both D- and B-configuration observations the PdBI was used with all six antennas available (15 independent baselines). The correlator consists of eight independent units each of which was covering 320 MHz (128 channels each with a width of 2.5 MHz) with a single polarization, covering a total bandwidth of about 1 GHz with both polarizations. Observations were tuned at a central frequency of 91.375 GHz for a total velocity bandpass of about 3000 km s^{-1} . For calibration of the data we observed standard bandpass calibrators (J0418+380, 3C273), phase/amplitude calibrators (J1044+719, J1150+497), and flux calibrators (MWC 349, 3C273) to which we regularly switched during the primary target observations. We reduced the data with the GILDAS software packages CLIC and MAP. The maps of the fields obtained using natural weights and using the full 1 GHz bandpass have noise levels of about $67.9 \mu\text{Jy beam}^{-1}$ and $51.2 \mu\text{Jy beam}^{-1}$ for the D- and B-configuration data, respectively.

Daddi et al. (2008) presented the CO[2–1] detection of the BzK galaxy with the D-configuration data. In addition to the BzK galaxy, from the initial D-configuration observations we also found a strong, serendipitous source in the field, located $22''$ south and $8''$ east of the primary target (Figure 1). Even when averaging all available channels over the 3000 km s^{-1} spectral range observed, and after subtracting from the data the signal from the primary target, the serendipitous source was securely detected, despite the large primary beam attenuation (PBA) at its distance from phase center (the primary beam results in an approximately Gaussian response with full width at half-maximum (FWHM) of $55''.2$ at this frequency). For this reason, for the follow-up observations in the more extended B configuration we offset the pointing by $10''$ from the BzK galaxy in order to reduce the PBA at the position of the serendipitous detection without compromising the data quality at the position of the primary target. In addition to confirming this serendipitous source, the new observations also revealed a second source at high significance (Figures 2 and 3), and a third tentative detection. The two secure detections correspond well to the positions of GN20 and GN20.2 in the sample of SMGs published in P06. In both cases, it is clear that most of the detected signal comes from an emission line, most likely from CO molecular gas.¹¹ Measured quantities are summarized in Tables 1 and 2 and derived quantities (like luminosities and masses) are in Table 3.

Table 1
Radio and CO Coordinates of the Sources

ID	R.A. _{CO} (J2000)	Decl. _{CO} (J2000)	R.A. _{VLA} (J2000)	Decl. _{VLA} (J2000)
GN20	12:37:11.90	62:22:12.1	12:37:11.89	62:22:11.8
GN20.2a	12:37:08.77	62:22:01.7	12:37:08.78	62:22:01.8
GN20.2b	12:37:09.73	62:22:02.6

Notes. CO coordinates are from our $1''.3$ beam, B-configuration observations of CO[4–3]. The VLA coordinates are from the 1.4 GHz radio continuum map of G. Morrison et al. 2009 (in preparation) with $1''.7$ beam.

2.1. CO Detection of GN20

GN20 is very securely detected in both D- and B-configuration observations (Figure 1 (left)). Most of the signal appears to be due to a CO emission line. Averaging the signal from 150 km s^{-1} to 900 km s^{-1} (here and in the following all velocities are defined with respect to the central frequency of the observations at 91.375 GHz) results in a detection with signal-to-noise ratio (S/N) = 10 for the D-configuration data (Figure 1 (left) and Figure 3 (top)). The B-configuration observations within the same velocity range result in a detection with $S/N = 13$ and a position of $\alpha(J2000) = 12^{\text{h}}37^{\text{m}}11^{\text{s}}.90$, $\delta(J2000) = 62^{\circ}22'12''.1$ (Figure 1 (left)). This position is consistent with the $7''$ submillimeter error box of the SMG GN20 (P06), and is within $0''.5$ of the accurate interferometric Iono et al. (2006) submillimeter-array (SMA) detection of this source and of the radio counterpart in 20 cm VLA data (G. Morrison et al. 2009, in preparation; Figure 4). The PdBI position coincides well with a faint galaxy that P06 already identified with the optical counterpart of GN20 (Figure 5). GN20 is the brightest SMG in the GOODS-N area. The radio, CO, and SMA submillimeter positions actually appear to be slightly offset to the east of the source seen in the optical (by $\sim 0''.5$ or so), as also noted by Iono et al. (2006). It is not clear if this is due to some additional galactic structure being present but extremely obscured, or just a random fluctuation across the data sets.

The PdBI D- and B-configuration data sets were independently fitted with a point source and the resulting spectra were corrected for PBA and co-added with appropriate weighting (the D-configuration observations are noisier on an absolute flux scale, also due to the larger correction for PBA). We performed Gaussian fitting of the resulting spectrum (Figure 3) to determine the CO line properties, allowing for the presence of a faint underlying continuum. The best-fitting Gaussian line is offset by $580 \pm 40 \text{ km s}^{-1}$ relative to the central frequency, and has an velocity integrated flux of $I_{\text{CO}} = 1.5 \pm 0.2 \text{ Jy km s}^{-1}$, with both errors given at the 1σ level and following Avni (1976) for the case of two parameters of interest (line velocity and integrated emission line flux). There is evidence for faint 3 mm continuum as well, as shown in Figure 1 (right panels) and Figure 3. To confirm this result, we averaged the signal in UV space for velocities outside a 1200 km s^{-1} range centered on the line (about $1.7 \times \text{FWHM}$), where negligible line contribution should be present. The resulting continuum map has a faint source at a position consistent within the errors with that of the emission line and corresponding to a signal of 0.33 mJy , significant at the 5σ level. To our knowledge, this is the first secure dust continuum detection of an SMG in the 3 mm band.

2.2. CO Detection of GN20.2a

Averaging the velocity channels between -300 km s^{-1} and 825 km s^{-1} a source is detected in the PdBI map with $S/N =$

¹¹ It is unlikely that the emission line is not from CO, given that CO lines are the brightest lines observed at millimeter wavelengths.

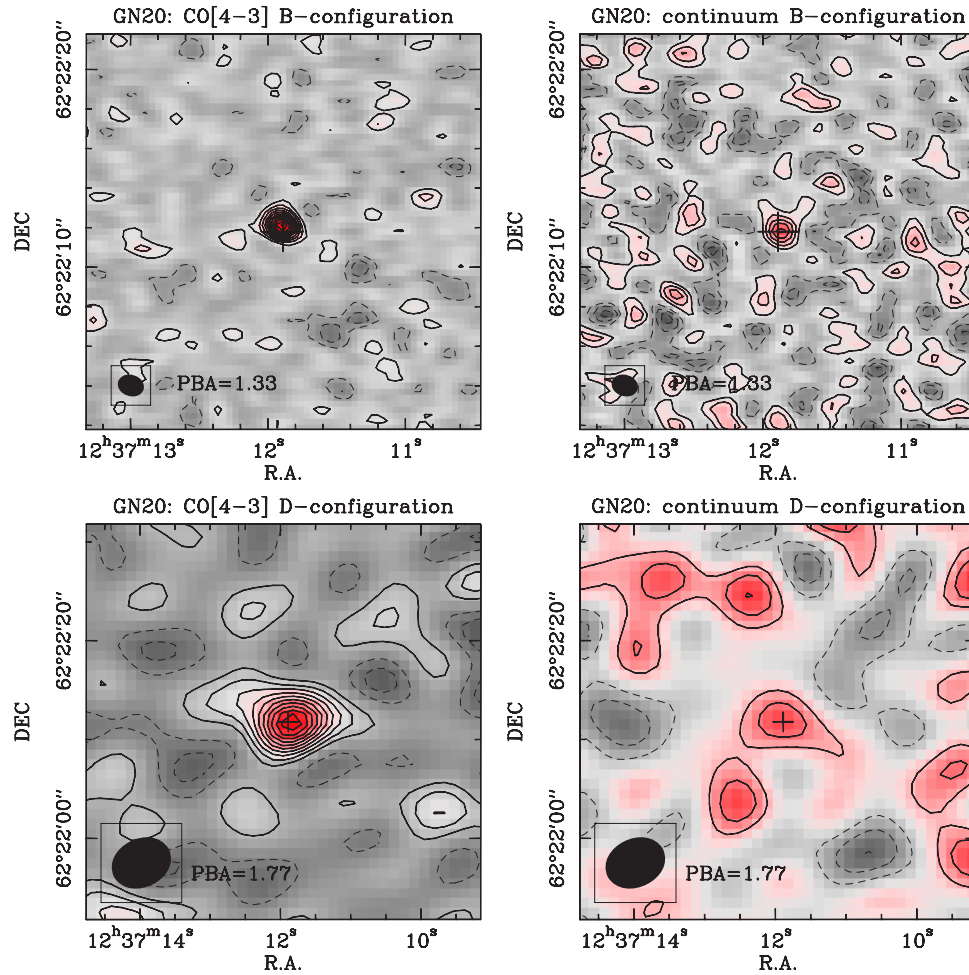


Figure 1. Velocity averaged spatial maps at 91.4 GHz centered on the serendipitously detected emission from GN20 (the 2'' wide cross refers to the VLA 1.4 GHz position). The two top panels show B-configuration 1'3 beam maps (20'' field of view) while the bottom panels show the D-configuration 5'5 beam maps (40'' field of view). Red colors correspond to positive fluxes and gray colors to negative fluxes. Contours level are shown in steps of 1σ with positive (negative) contours shown as solid (dashed) lines. The CO[4–3] maps are averaged over 750 km s^{-1} corresponding to the observed range of CO emission (see Figure 3) and were cleaned. The continuum maps show the average of all channels outside the line range (for a 2250 km s^{-1} total bandpass). Note that GN20 is observed away from the phase center with PBA (labeled in each image) of 1.33 and 1.77 at its position in the B- and D-configuration observations (these maps were not corrected for attenuation in order to preserve the flatness of the noise). Given the relatively low S/N, the continuum maps were not cleaned as the side lobes are below the noise level.

(A color version of this figure is available in the online journal.)

Table 2
Measured Properties of GN20, GN20.2a and GN20.2b

ID	z_{CO}	z_{Keck}	$S_{850 \mu\text{m}}$ (mJy)	$S_{3.3 \text{ mm}}$ (mJy)	$S_{1.4 \text{ GHz}}$ (μJy)	$S_{24 \mu\text{m}}$ (μJy)	$S_{8.0 \mu\text{m}}$ (μJy)	$S_{4.5 \mu\text{m}}$ (μJy)	$I_{\text{CO}[4-3]}$ (Jy km s ⁻¹)	FWHM (km s ⁻¹)
(1)	(2)	(3)	(4)	(5)	(6)	(7)	(8)	(9)	(10)	(11)
GN20	4.055 ± 0.001	4.06 ± 0.02	$20.3 \pm 2.1^\dagger$	0.33 ± 0.07	75.8 ± 7.9	65.5 ± 3.5	26.1 ± 2.6	9.5 ± 1.0	1.5 ± 0.2	710 ± 120
GN20.2a	4.051 ± 0.003	4.059 ± 0.007	$<9.9 \pm 2.3^\dagger$	<0.20	$180.7 \pm 8.4^\dagger$	30.2 ± 5.6	9.8 ± 1.0	4.1 ± 0.4	0.9 ± 0.3	1100 ± 400
GN20.2b	$<9.9 \pm 2.3^\dagger$	<0.18	32.2 ± 6.5	12.0 ± 4.3	15.4 ± 1.5	10.1 ± 1.0

Notes. Column 1: name of the object. Column 2: redshift derived from the CO[4–3] observations. Column 3: redshift derived from the Keck optical spectroscopy. Column 4: SCUBA 850 μm flux density from P06[†]. Column 5: continuum flux density at 3.3 mm. We note that only GN20 is detected in the 3.3 mm continuum. For GN20.2a and GN20.2b we list 2σ upper limits. The formal 3.3 mm continuum measurement are 0.11 ± 0.10 and 0.08 ± 0.09 , respectively. Column 6: VLA 1.4 GHz flux density from P06[†] and our own measurements. Column 7: *Spitzer*+MIPS 24 μm flux density. Columns 8 and 9: *Spitzer*+IRAC flux densities. All detections have high significance, errors are dominated by systematics effects at the 10% level. Column 10: velocity integrated CO[4–3] flux. Column 11: width of CO[4–3] line, estimated through a single Gaussian fitting.

5.8 at the position of $\alpha(J2000) = 12^{\text{h}}37^{\text{m}}08^{\text{s}}.77$, $\delta(J2000) = 62^{\circ}22'01''.7$ in the B-configuration observations (Figure 2 (left) and Figure 3 (right)). Positive flux with S/N just below 3 is also observed in the D-configuration data at this position (Figure 2 (left)). We extracted the spectra by fitting point sources in the D- and B-configuration data sets independently and co-

added the spectra with weighting after correcting for PBA. Averaging the total resulting spectrum within -300 km s^{-1} and 825 km s^{-1} , we find a positive signal significant at the 7σ level.

The position of this source is within 0'.2 of the relatively bright radio source that P06 identified with the counterpart of the SMG

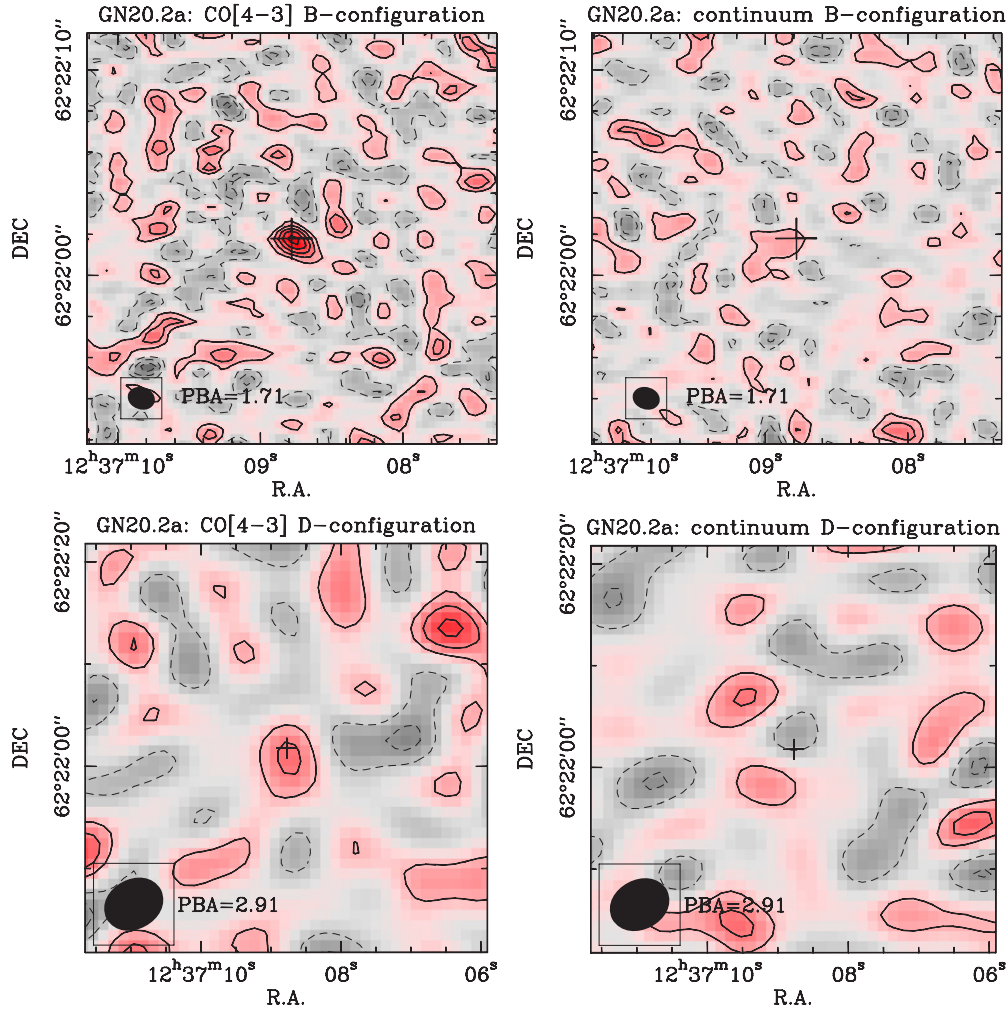


Figure 2. Same as Figure 1 but for the galaxy GN20.2a (the $2''$ wide cross refers to the VLA 1.4 GHz position). The CO[4–3] maps are averaged here over 1125 km s^{-1} corresponding to the observed range of CO emission for GN20.2a (see Figure 3). The continuum maps show the average of all channels outside the line range (for a 1875 km s^{-1} total bandpass). GN20.2a is even more offset than GN20 from the phase center with PBA (labeled in each image) of 1.71 and 2.91 at its position in the B- and D-configuration observations. Before creating these maps, the bright emission at the position of GN20 was fitted in the uv data with a point source model and subtracted, in order to avoid contamination at the position of GN20.2 from the side lobes of the more luminous GN20 galaxy. These maps were not cleaned as the side lobes are below the noise level in all cases. No correction for PBA is applied to these maps, in order to preserve the flatness of the noise.

(A color version of this figure is available in the online journal.)

Table 3
Derived Properties of GN20 and GN20.2a

ID	L_{IR} (L_{\odot})	$L'_{\text{CO}[4-3]}$ ($\text{K km s}^{-1} \text{ pc}^2$)	$L_{1.4 \text{ GHz}}$ (W Hz^{-1})	M_{stars} (M_{\odot})	M_{gas} (M_{\odot})	M_{dyn} ($\sin i^{-2} M_{\odot}$)
(1)	(2)	(3)	(4)	(5)	(6)	(7)
GN20	2.9×10^{13}	6.2×10^{10}	8.4×10^{24}	2.3×10^{11}	5.0×10^{10}	2.3×10^{11}
GN20.2a	1.6×10^{13}	3.7×10^{10}	2×10^{25}	0.5×10^{11}	3.0×10^{10}	...

Notes. Column 1: name of the object. Column 2: total IR luminosities for GN20 and GN20.2a are derived by fitting the global IR SED using all available flux density measurements from 24μ to 1.4 GHz with CE01 models. For GN20.2a, the 1.4 GHz measurement was not used, as it is affected likely by an AGN, and we attributed the whole $850 \mu\text{m}$ emission to this source. Typical errors are estimated to be of the order of 0.2 dex and 0.3 dex for GN20 and GN20.2a, respectively. Column 3: luminosity of the CO[4–3] transition. Column 4: 1.4 GHz rest-frame luminosities, estimated using a radio continuum index $\alpha = 0.8$ ($f_{\nu} \propto \nu^{-\alpha}$), $L_{1.4 \text{ GHz}} = 4\pi D_L^2 S(1.4 \text{ GHz})(1+z)^{-0.2}$ (D_L is the luminosity distance). Column 5: stellar masses are estimated from SED fitting from HST+ACS to *Spitzer*+IRAC photometry, using constant SFR models from Maraston (2005) and allowing for dust reddening with a Calzetti et al. (2000) law. Typical errors are found to be about 0.2 dex. Column 6: molecular gas masses assume that the CO[1–0] and CO[4–3] transitions correspond to the same brightness temperature and a conversion factor $X_{\text{CO}} = 0.8 M_{\odot} (\text{K km s}^{-1} \text{ pc}^2)^{-1}$. Column 7: the dynamical mass for GN20 is estimated following Solomon & Vanden Bout (2005) using $M_{\text{dyn}} \times \sin^2 i / M_{\odot} = 233.5 \times v_{\text{FWHM}}^2 \times r_e$ (with velocity expressed in km s^{-1} and half light radius in pc).

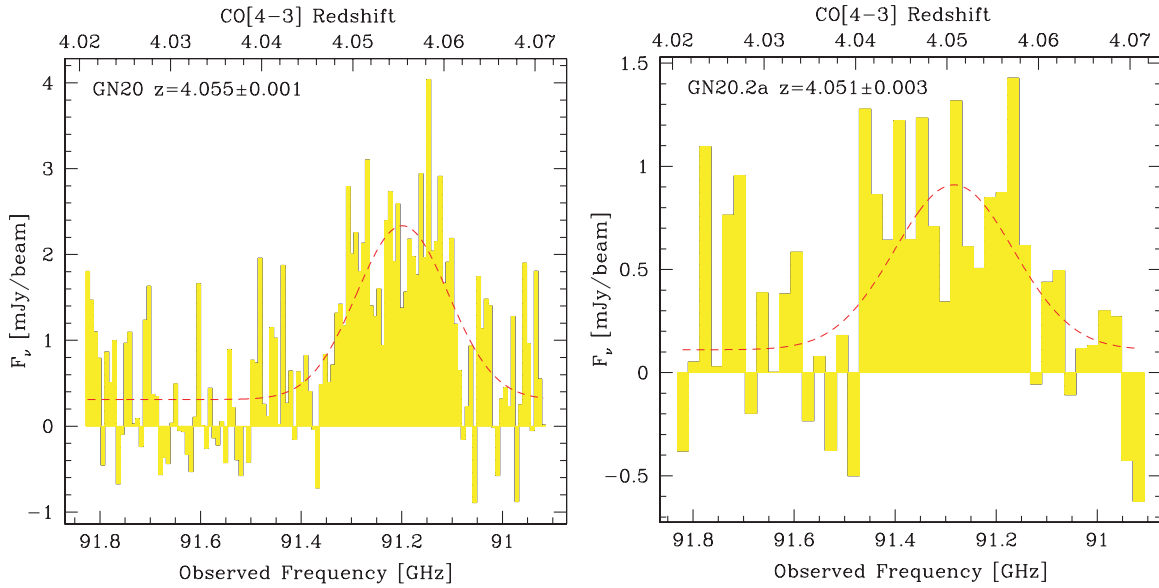


Figure 3. One-dimensional spectra of CO[4–3] from GN20 (left, sampled at 25 km s^{-1}) and GN20.2a (right, sampled at 75 km s^{-1}). The flux densities have been corrected for PBA. The red curve shows the best-fitting Gaussian to the measured signal, allowing for the presence of faint underlying continuum. (A color version of this figure is available in the online journal.)

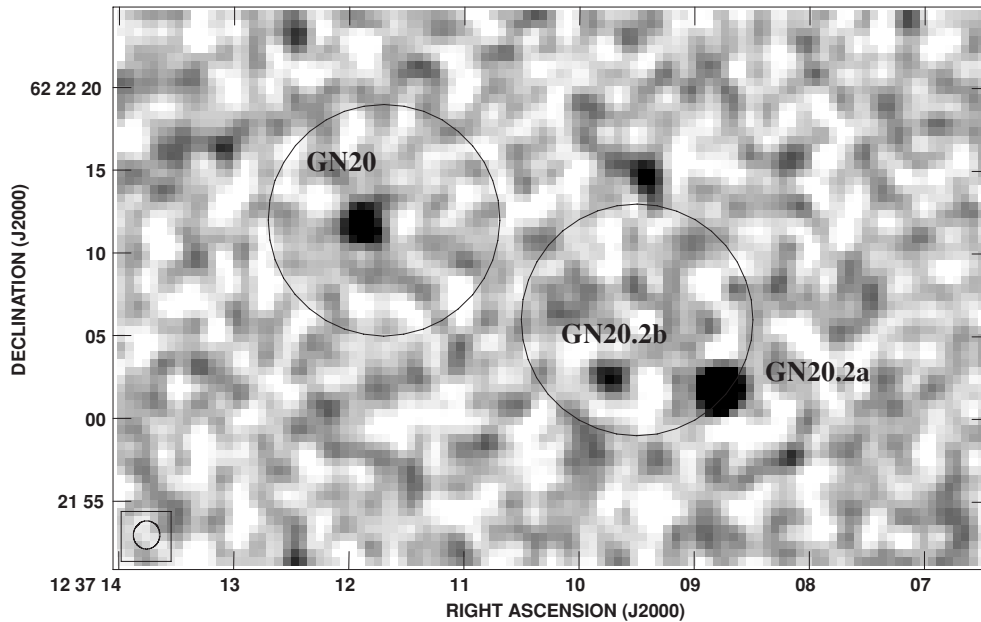


Figure 4. VLA 1.4 GHz radio continuum map of the GN20 (left) and GN20.2 (right) region. The VLA observations were mostly taken in A-array and have a beam of $1''.7$ FWHM (G. Morrison et al. 2009, in preparation). The $7''$ radii circles are centered on the SCUBA positions from P06. The radio sources within the $850 \mu\text{m}$ beam are labeled. The faint radio emission about $1''$ north of the GN20.2 SCUBA beam is real and corresponds to a galaxy with $z_{\text{phot}} = 1.6$. From its mid-IR emission, we infer only moderate SFR levels that should not be substantially contributing to the flux density observed at submillimeter wavelength at the position of GN20.2.

GN20.2, close but well distinguished from GN20 that is $24''$ to the NE. The position corresponds to a faint galaxy in the deep *Hubble Space Telescope* (HST) images (Figure 5). Also in this case the signal appears to be mostly due to an emission line. The best-fitting Gaussian line is offset by $330 \pm 150 \text{ km s}^{-1}$ relative to the central frequency, and has a velocity integrated flux of $I_{\text{CO}} = 0.9 \pm 0.3 \text{ Jy km s}^{-1}$. The largest contribution to the flux error is the uncertainty in the continuum level. Some positive continuum appears to be present, although the S/N is not yet sufficient for a reliable measurement (Table 2). Accounting for the possible continuum emission and its uncertainty, the CO emission line is still detected at the 6σ level.

2.3. GN20.2b: a Second Counterpart to GN20.2?

Inspection of the newly reprocessed 1.4 GHz radio map around the position of GN20.2 (Figure 4; G. Morrison et al. 2009, in preparation) shows an additional faint radio source with a flux density of $32.2 \mu\text{Jy}$ (5σ) at $\alpha(J2000) = 12^{\text{h}}37^{\text{m}}09^{\text{s}}.73$, $\delta(J2000) = 62^{\circ}22'02''.6$ (radio frame), $3''.4$ from the GN20.2 SCUBA position (P06) and $6''.8$ from the CO-detected counterpart discussed above. We refer to the primary counterpart of GN20.2 as GN20.2a, and this newly identified faint radio source is referred to as GN20.2b. GN20.2b is a plausible additional counterpart to the submillimeter emission.

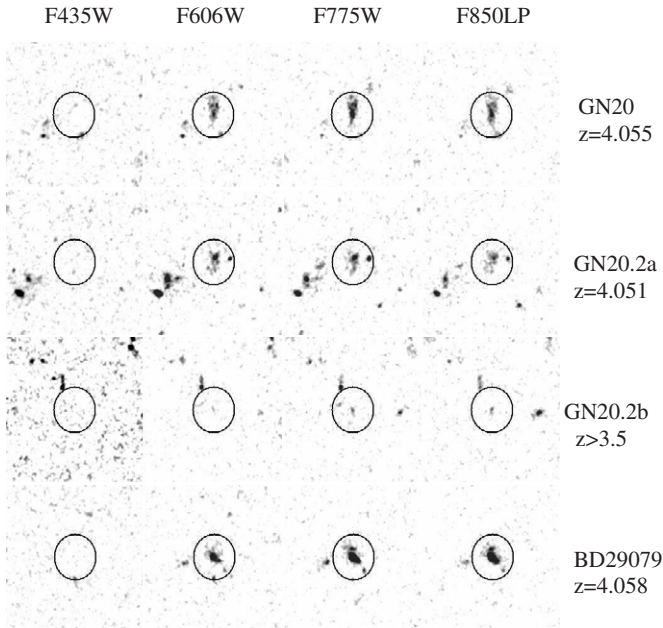


Figure 5. Multiband *HST*+ACS imaging of the optical counterparts of GN20 (top), GN20.2a (second from top), GN20.2b (third from top), and a B-dropout Lyman break galaxy in the area having also $z_{\text{spec}} = 4.058$ from Keck spectroscopy (the coordinates of this source, named BD29079 in the GOODS-N B-dropout catalog, are $\alpha(J2000) = 12^{\text{h}}37^{\text{m}}11^{\text{s}}.53$, $\delta(J2000) = 62^{\circ}21^{\text{m}}55^{\text{s}}.7$). From left to right, as labeled, the data refer to the ACS filters F435W, F606W, F775W, and F850LP (sometimes referred to in the text also as B , v , i and z bands, respectively). The images have been smoothed with a 3 pixel FWHM Gaussian. Circles around the sources have $1''$ radius and are simply centered on the identified ACS counterparts.

Interestingly, positive signal is found in the PdBI map close to the position of GN20.2b. The PdBI D- and B-configuration data sets were independently fitted with a point source fixed at the VLA position of GN20.2b (a secure position cannot be derived from the PdBI data alone, due to the low S/N) and the resulting spectra were corrected for PBA and co-added, weighting according to the noise, similarly to what was done for the other galaxies. Averaging over the whole 1 GHz bandwidth in the co-added spectrum results in a $\sim 3\sigma$ signal. If we average the spectrum between $\approx 0 \text{ km s}^{-1}$ and $\approx 700 \text{ km s}^{-1}$, we find a $> 4\sigma$ signal. Although longer integrations at PdBI would be required for a more reliable conclusion, the data are again consistent with CO emission, quite close in frequency to the other securely detected lines. If real, that would correspond to an integrated flux of $I_{\text{CO}} \approx 0.45 \text{ Jy km s}^{-1}$.

3. REDSHIFT IDENTIFICATIONS

Depending on which transition we are actually observing, the CO detection fixes the redshift of GN20 and GN20.2a to $1 + z_{\text{CO}} \sim 1.264 \times n$, where the observed transition is $\text{CO}[(n) - (n - 1)]$. Possible redshifts are 0.26, 1.53, 2.80, 4.05, 5.32, 6.58, etc. The most straightforward guess for the redshift would be 1.53, corresponding to companion galaxies to BzK-21000, the primary target of the PdBI observations. However, we show in the following that the correct identification for the lines is $\text{CO}[4-3]$ at redshift $z_{\text{CO}} \sim 4.05$, making these among the most distant CO detections so far for SMGs. Although it might seem unlikely that we have serendipitously detected CO emission lines from $z \gtrsim 4$ galaxies, we note that the 1 GHz spectral range of our data maps into a twice larger redshift range at $z \sim 4$ versus $z \sim 1.5$, which in turn corresponds to

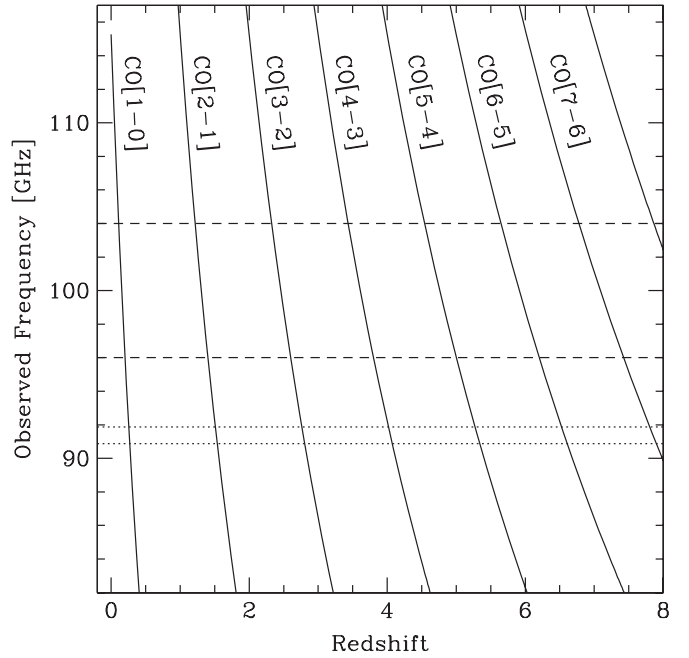


Figure 6. Frequency-redshift relation for CO emission lines in the 3 mm atmospheric window. The dotted range around 91.4 GHz corresponds to the PdBI observations presented in this paper. The dashed line centered at 100 GHz corresponds to an 8 GHz range, as planned for future generations of correlators, like those that will be used on ALMA.

a two times larger comoving volume. Also, at higher redshift the density of CO transitions per unit frequency and at fixed observed frequency is higher, hence chance detections are non-negligible once a luminous high-redshift target is within the field of view (Figure 6).

The following section discusses several independent redshift estimates for these galaxies, e.g., based on optical photometric redshifts, radio-IR photometric redshifts, and optical spectroscopy. This comparison is interesting as the problem of unidentified CO line detections will become a typical situation of the coming years with new, wide-band instrumentation rapidly becoming available. Even 8–20 GHz receivers will often identify single CO lines from single galaxies (Figure 6). A direct assessment and intercomparison of multiple redshift identification techniques is thus interesting for this first test case of serendipitously detected CO lines.

3.1. GN20

3.1.1. Photometric Redshift from Stellar Emission

Figure 5 shows *HST*+ACS imaging in the four bands available in GOODS (Giavalisco et al. 2004a). As already noted by P06, the optical counterpart of GN20 is a B-dropout Lyman break galaxy according to the definition of Giavalisco et al. (2004b). This definition returns galaxy samples with $z = 3.78 \pm 0.34$, favoring the identification of the PdBI line as $\text{CO}[4-3]$ at $z = 4.055$. Circumstantial evidence for the likelihood of a redshift around $z = 4.05$ had been even earlier presumed from the presence of a bright B -band dropout galaxy at a $16''$ separation (Figure 5) with fairly similar colors and a known spectroscopic redshift of $z = 4.058$ measured from Keck spectroscopy (D. Stern et al. 2009, in preparation; we refer to this object as BD29079). The IRAC colors of the GN20 B -band dropout counterpart are very red, with the brightest IRAC band being the $8.0 \mu\text{m}$ (see e.g., P06). If due to the emission of

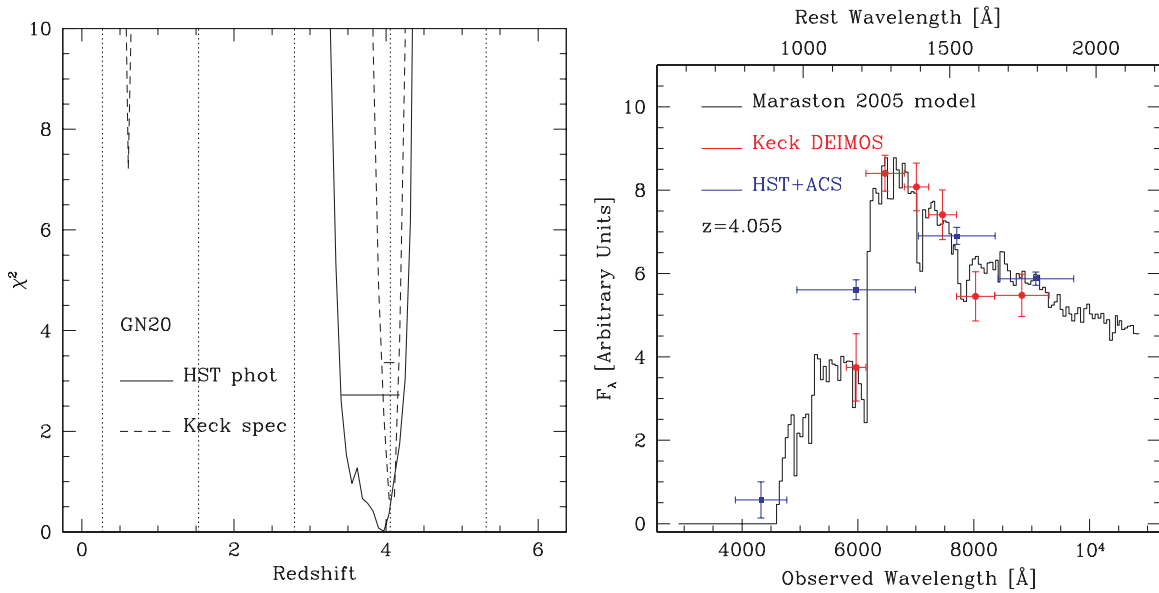


Figure 7. Left panel: photometric redshifts from stellar emission for the optical counterpart of GN20. The solid line shows the result of fitting the UV rest-frame continuum *HST* photometry described in Section 3.1.1, while the dashed line refers to the fit of the binned Keck+DEIMOS spectroscopy discussed in Section 3.1.3. The dotted horizontal lines show the permitted redshifts, based on the detection of CO emission. Right panel: the optical SED of GN20 as derived from *HST*+ACS imaging (blue points) and Keck spectroscopy (after binning in wavelength; red points). A strong break at about 6150 Å is observed, corresponding to the Ly α forest break at $z = 4.055$.

(A color version of this figure is available in the online journal.)

stars, this implies that the 1.6 μm rest-frame bump is beyond the 5.8 μm channel, or $z \gtrsim 3.5$. However, the IRAC emission can also be red due to, or affected by, the presence of obscured active galactic nuclei (AGNs; e.g., Stern et al. 2005; Daddi et al. 2007b).

Stellar photometric redshifts were thus estimated using only the four *HST* bands and running the *hyperz* code (Bolzonella et al. 2000). The Maraston (2005) models were used, with a variety of star formation histories and allowing for reddening using the Calzetti et al. (2000) law. The near-IR bands are not used because the available data sets, described, e.g., in Daddi et al. (2007a), are not sufficiently deep to place meaningful constraints on the spectral energy distribution (SED) of this faint and relatively blue galaxy. The distribution of χ^2 values versus redshift (Figure 7) is consistent with $3.4 < z < 4.2$ (95% confidence range). Figure 7 shows the observed SED and the best-fitting model for the case of $z = 4.055$.

3.1.2. Photometric Redshift from the Infrared and Radio Emission

An independent estimate of the redshift of GN20 can be derived from its FIR emission. The ratio between mid-IR, FIR, mm, and radio flux densities is redshift dependent. Locally, the radio luminosity is observed to be proportional to the bolometric IR luminosity (Condon 1992; Yun et al. 2001), and this seems to hold at high redshift as well (Elbaz et al. 2002; Garrett 2002; Appleton et al. 2004). However, the *K*-corrections at radio and FIR wavelengths are very different, and thus the radio/FIR flux ratio depends strongly on redshift. Originally this idea was exploited by Carilli & Yun (1999, 2000) to estimate photometric redshifts of distant SMGs, also attempted by several other studies (Hughes et al. 2002; Wiklind 2003; Aretxaga et al. 2003, 2005, 2007; Clements et al. 2008). In addition, one can exploit the fact that the mid to FIR emission has a generally well-defined peak at 50–200 μm , affecting directly the ratio of mid-IR to submillimeter and millimeter emission.

For this purpose, we use the available photometry at 24 μm , 850 μm , 3 mm, and 20 cm. Some of the *Spitzer*+MIPS 24 μm and VLA 20 cm measurements are updated from P06 using the most up-to-date GOODS data sets. We measure a 24 μm flux density of $65.5 \pm 3.5 \mu\text{Jy}$ and a 20 cm flux density of $75.8 \pm 7.9 \mu\text{Jy}$. We use a 850 μm flux density of $20.3 \pm 2.3 \text{ mJy}$ from P06 and a 3.3 mm flux density of $0.33 \pm 0.07 \text{ mJy}$ (Section 2).

The observed flux densities have been compared, as a function of redshift, to the predictions of a suite of 105 template SEDs that were built following the luminosity correlations observed for local galaxies as described in Chary & Elbaz (2001). The template dust temperatures get warmer with increasing luminosity from a minimum template luminosity of $\text{Log } L_{\text{IR}}/L_\odot = 8.41$ up to a maximum luminosity of $\text{Log } L_{\text{IR}}/L_\odot = 13.55$. Radio continuum emission is added to each template following the radio–IR correlation (Yun et al. 2001). For each template of a given luminosity, we compute the expected flux densities in the available bands (24 μm , 850 μm , 3 mm, and 20 cm) as a function of redshift and perform a χ^2 minimization over the template total IR luminosity as a function of redshift, without allowing the template normalizations to vary. In order to avoid biasing the fitting to a particular band, we increased the formal uncertainty in the 24 μm flux density in order to reduce the S/N from 20 to 9, comparable to the radio and submillimeter bands.

Figure 8 shows the results. The best-fitting redshift is $z_{\text{phot}} = 3.7$ and the 99% confidence interval is $3.3 < z < 4.3$. Therefore, we conclude that the radio–IR SED also independently supports the $z = 4.055$ redshift determination. We note that this analysis allows us to reject with high confidence any redshift identification with $z < 3$ or $z > 5$.

Figure 8 (right panel) also shows the comparison of the observed GN20 SED from UV to radio to the best-fitting (and brightest) template in the library of Chary & Elbaz (2001). The SED is remarkably well reproduced in the mid- to far-infrared and radio, without any rescaling or ad hoc normalizations.

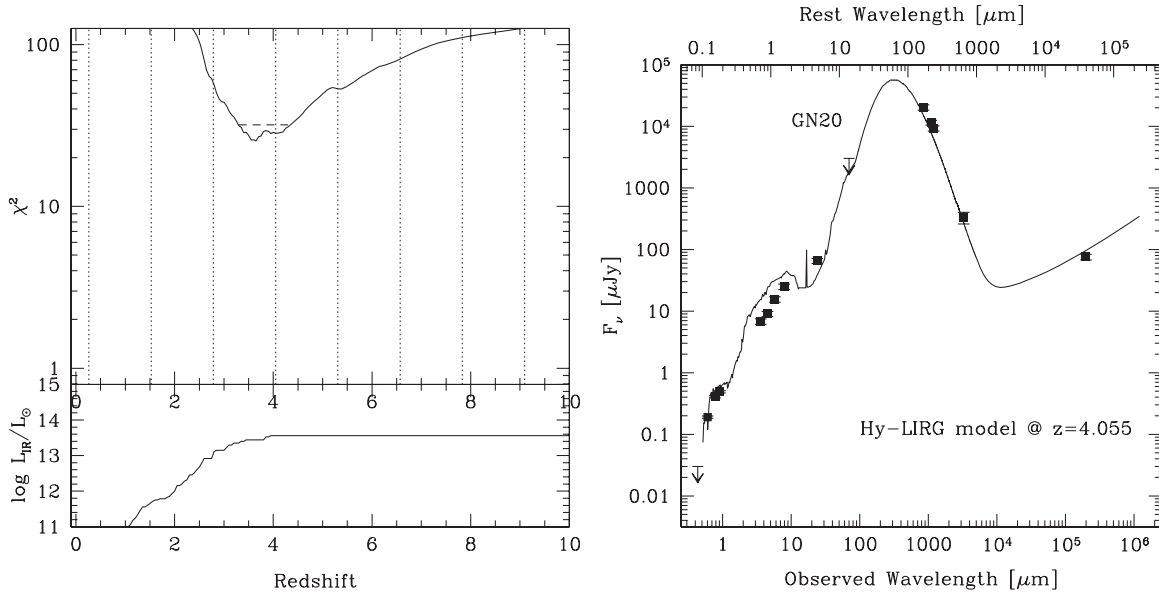


Figure 8. Left panel: χ^2 vs. redshift for the radio-IR fitting of GN20, based on the 24 μm , 850 μm , 3 mm, and 20 cm observed flux densities and the CE01 library of template galaxies. Right panel: the SED of GN20. The brightest CE01 model with $L_{\text{IR}} = 3.5 \times 10^{13} L_{\odot}$ is overplotted for comparison, without any rescaling, redshifted to $z = 4.055$. This is very close to the best-fitting photometric redshift solution at $z_{\text{phot}} = 3.7$. We also show here the 1.1 mm and 1.2 mm flux density measurements recently published by Perera et al. (2008) and Greve et al. (2008). GN20 is undetected in the 70 μm *Spitzer*+MIPS imaging by Frayer et al. (2006) and we show an upper limit of 3 mJy.

The UV-optical part of the template SED also happens to match the shape of the observed data quite well, although there is a factor of ~ 2 offset over the IRAC bands that implies a different $L(\text{FIR})/L(\text{optical})$ ratio, suggesting a higher specific star formation rate (SSFR). A similarly good agreement, including the optical/UV portion of the SED, was seen by Daddi et al. (2005b) when comparing the average SED of $z = 2$ BzK-selected ultraluminous infrared galaxies (ULIRGs) to Chary & Elbaz (2001) templates. The optical/UV emission was simply added to the models using a synthetic stellar population model matched to the Arp220 SED and scaled to reproduce the local broad correlation between bolometric luminosity and *B*-band rest-frame luminosity.

3.1.3. Keck Spectroscopy

A solid identification of the CO line, and thus a determination of GN20's redshift, is finally provided by deep optical spectroscopy. The counterpart of GN20 was observed with the Deep Imaging Multi-Object Spectrograph (DEIMOS; Faber et al. 2003) on the Keck II telescope several times between 2004 and 2007, though only the final observations on UT 2007 April 14–15 were taken in good conditions. The total integration time was 2.5 hr, and a $1''.2$ wide slit was oriented along the major axis of the galaxy (P.A. = $13^\circ 8$). The 600ZD grating ($\lambda_{\text{blaze}} = 7500 \text{ \AA}$) was used, providing a resolution $R = 2000$. The GG455 order-blocking filter was installed. We processed the data using a slightly modified version of the DEEP2 DEIMOS pipeline.¹²

The data show no emission lines while the continuum has a low S/N per pixel, as expected given the faintness of the source ($i \sim 25$) and its spatial extent of about $1''.5$, implying a low surface brightness. The emission is nevertheless clearly seen after smoothing the spectrum. We extracted the galaxy spectrum with *apall* under IRAF using a $1''.2$ wide aperture. We measured the rms per pixel as a function of wavelength based on

the sky spectrum. This information was used to properly weight pixels when binning by wavelength (e.g., to down-weight noisy pixels affected by OH sky lines) and to accurately estimate the error of the binned spectrum. Given that for $z = 4.055$ the $\text{Ly}\alpha$ forest break would fall at 6145 \AA , we included two spectral bins bracketing this wavelength to verify if a break is indeed present as expected. Figure 7 (right panel) shows the results. Although the Keck spectrum only extends down to 5900 \AA , and therefore only one binning point is available with decent S/N below the expected $\text{Ly}\alpha$ forest break, we find that the spectrum strongly supports the $z = 4.055$ redshift and in particular it reveals the presence of the expected $\text{Ly}\alpha$ forest break. The flux density measurement blueward of the expected break corresponds to a $\text{Ly}\alpha$ forest decrement of $D_A = 0.55 \pm 0.10$ (derived using the stacked bins closer to the break), fully consistent to what is expected for the mean transmission of the intergalactic medium at $z = 4.05$ (Songaila 2004). When running a photometric redshift analysis on the binned Keck+DEIMOS data (Figure 7, left panel) we see that of the possible CO line transition identifications the $z = 4.055$ redshift is unambiguously chosen with very high confidence.

3.2. GN20.2a

A nearby ($24''$ separation; 169 kpc proper distance at $z = 4.05$) SMG companion to GN20 is GN20.2, first discovered by Chapman et al. (2001).¹³ GN20.2 has an 850 μm flux density of 9.9 mJy as reported by P06, who also identifies the most likely optical counterpart with a relatively bright radio source ($S(20 \text{ cm}) = 180 \mu\text{Jy}$). This galaxy is also a B-dropout (P06; Figure 5) with a faint 24 μm flux density of $30.2 \mu\text{Jy}$.

An analysis similar to the one performed in Section 3.1 results in a photometric redshift of $z_{\text{phot,opt}} = 3.93$ and a 90% confidence range within $3.55 < z < 4.05$. Similarly, the

¹² See <http://astron.berkeley.edu/~cooper/deep/spec2d/>.

¹³ Chapman et al. (2001) used SCUBA to observe (and successfully detect) objects from a sample of optically faint radio sources with $I > 25$ mag. GN20.2, alias VLA J123708+622201, was part of this survey.

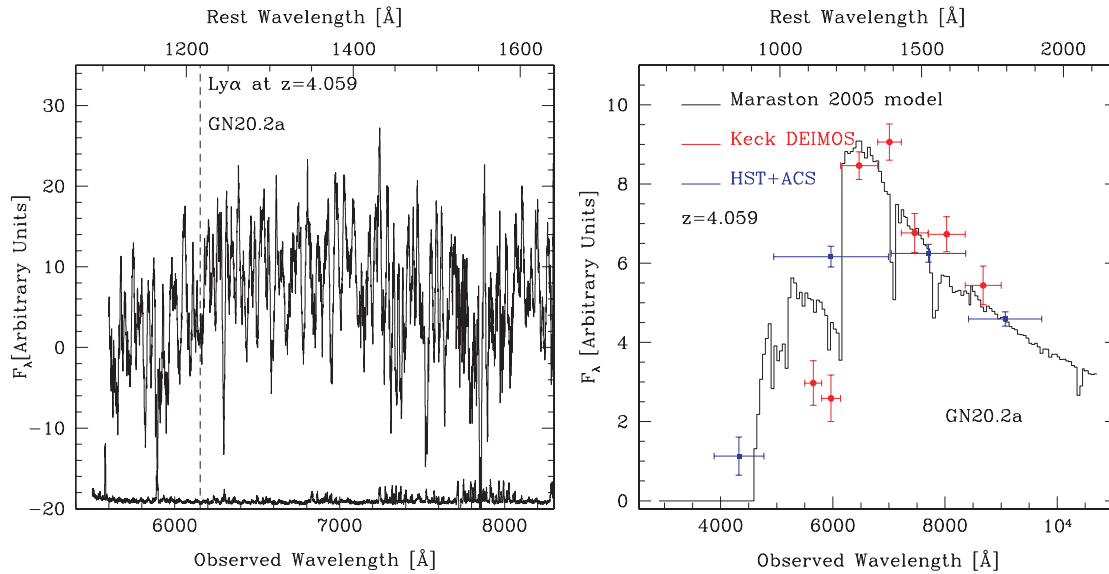


Figure 9. Keck spectroscopy results for the GN20.2a optical counterpart. The left panel shows the Keck spectrum, smoothed with a 17 Å boxcar (27 pixels) in order to increase the S/N. The Ly α forest break is well detected, yielding a redshift of $z = 4.059 \pm 0.007$ (1σ , determined from spectral fitting with a Maraston [2005; M05] template). This is consistent with $z = 4.051 \pm 0.003$ derived from the CO emission. The relative sky noise vs. wavelength is shown at the bottom of the plot. The right panel is as in Figure 7, but for the GN20.2a galaxy, showing the binned Keck spectra and the *HST* photometry. The best-fitting M05 model is shown, redshifted to $z = 4.059$.

(A color version of this figure is available in the online journal.)

analysis of the IR SED suggests a redshift of $3.4 < z < 4.2$ at the 99% confidence. This confirms that the overall properties of this source are compatible with it being at the same redshift of GN20. This is further demonstrated by deep Keck+DEIMOS spectroscopy (2.5 hr) of this galaxy that was obtained in 2005 April during cirrus conditions, and reduced in the same way as for the GN20 observations (see Section 3.1.3). Figure 9 shows that a strong spectral break is detected at about 6150 Å, consistent with the location expected for the Ly α forest break at a redshift of 4.055. The observed break corresponds to a Ly α forest decrement $D_A = 0.67 \pm 0.05$, larger than the average expected value but still within the observed scatter in the intergalactic medium transmission at $z = 4.05$ (Songaila 2004). We constrain the redshift of this source to be $z = 4.059 \pm 0.007$ (1σ), based on fitting the Keck spectroscopy with the Maraston (2005) model shown in Figure 9, demonstrating that this source is at a similar redshift to that of its brighter companion GN20. We conclude that in this case the detected emission is also CO[4–3] at $z = 4.051 \pm 0.003$, in good agreement with the Keck spectroscopy.

3.3. GN20.2b: Redshift and Contribution to the Submillimeter Flux

The GN20.2b radio source is 3'4 from the GN20.2 SCUBA position of P06, closer than GN20.2a which is 6'0 away (although, we caution that the SCUBA position of GN20.2 might be less accurate than that for the average SMG, due to the brighter and nearby companion, GN20). The radio position is close (only 0'5 to the north) to a very faint galaxy ($z = 27.34$) detected in the *HST*+ACS imaging (Figure 5). It is possible that this faint radio galaxy could be at the same $z \sim 4.05$ redshift of GN20 and GN20.2a, and that it could be contributing some of the submillimeter flux detected at the position of GN20.2. We will discuss these two issues here in turn.

Although undetected in the *HST*/ACS F435W band, the faint ACS counterpart to GN20.2b is not formally classified as a

B-band dropout due to the upper limit in F435W not being stringent enough, but its blue ($i - z$) and red ($v - i$) colors support the hypothesis that this object is also at $z \sim 4$. The galaxy is also fairly bright and red at IRAC wavelengths (SED peak at 8.0 μ m with 20.93 mag) and is selected as a $z > 3.5$ massive galaxy candidate in the work of Mancini et al. (2009). Inspecting the highest resolution IRAC imaging at 3.6 μ m and 4.5 μ m, it appears that blending with a neighboring source is somewhat affecting the *Spitzer* IRAC measurements and biasing the flux densities high (likely by at most a factor of 1.5–2). We used the radio–IR photometric redshift technique to constrain its redshift, under the assumption that the emission is dominated by star formation and not an AGN. We find that by itself, the large ratio to 24 μ m flux density ratio for this source strongly constrains its redshift to $z > 3.2$ (99% confidence level), independently of how much it contributes to the 9.9 mJy flux density at 850 μ m. This is consistent with this object being an intrinsically very luminous, highly star-forming galaxy at high redshift (although, in principle, the high ratio could also be due to radio-loud AGN emission at a lower redshift). As discussed in Section 2.3, there is possible evidence for CO emission from this source, where a positive signal is found at the $> 4\sigma$ level. Although the situation is not secure as for the other two sources, we conclude that there is some supporting evidence for a similar $z \sim 4.05$ redshift also for GN20.2b. Taking the CO signal at face value, we would assign a redshift of $z = 4.052 \pm 0.006$ to GN20.2b, where the error corresponds to half the frequency range spanned by the tentative positive emission, if we identify that as CO[4–3]. This is within $\Delta z = 0.003$ of the redshift of GN20 and GN20.2a, while our data are sensitive in principle to emission from a redshift range that is 17 times wider, from $4.02 < z < 4.07$. We conclude that it is at least plausible that GN20.2b could be lying at a redshift similar to that of GN20.2a. In any case, this appear to be a fairly high-redshift ($z > 3.5$) galaxy.

Could GN20.2b be contributing some major fraction of the submillimeter flux of GN20.2? Finding multicomponent systems is not a new situation for SMG identification.

For example, SMMJ094303 (Tacconi et al. 2006) and GN19 (HDF242; Tacconi et al. 2008) are two cases where two-component systems, both radio detected, have been confirmed through CO observations. Dannerbauer et al. (2004), P06, Ivison et al. (2007), and Younger et al. (2008a) report other cases of submillimeter/millimeter galaxies with two radio counterparts. If this is also happening for GN20.2, it is not easy to assess quantitatively. Below we present circumstantial evidences in favor or against this hypothesis.

The main supporting evidence is that its VLA 1.4 GHz radio continuum flux density is $42\% \pm 10\%$ that of GN20, which is similar to the ratio between the submillimeter fluxes of the same two galaxies, suggesting that GN20.2b might be contributing some substantial flux, unless the radio emission is affected by an AGN. We note though that GN20.2b is 5.5 times fainter in the VLA 1.4 GHz radio continuum than GN20.2a, but this is likely due to the fact that the radio emission of GN20.2a (more than twice as bright as that of GN20) is powered by an AGN, as discussed in the following section.

There is, however, evidence against a major submillimeter flux contribution from GN20.2b. Comparing the $24 \mu\text{m}$ flux density measurements, we find that GN20.2b (only tentatively detected at $24 \mu\text{m}$) is at least 2–3 times fainter than GN20.2a and at least 5.5 times fainter than GN20. Accounting also for blending, the $S(24 \mu\text{m})/S(4.5 \mu\text{m})$ flux density ratios are at most a factor of 2 for GN20.2b and about factors of 6–7 for GN20 and GN20.2a (Table 2). This is evidence for lower SSFR in GN20.2b, suggesting that this galaxy has already passed its major peak of activity. Similarly, the ratio of the CO fluxes detected for GN20.2 and GN20.2a is roughly a factor of 2, similar to the ratio of submillimeter fluxes between the two galaxies (Table 2). Even if the tentative CO emission of GN20.2b is real, this would still be at most half of the CO emission of GN20.2a (but, of course, there could be stronger CO emission if the galaxy lies outside of the redshift range $4.02 < z < 4.07$). Given that the CO and bolometric luminosities of SMGs are known to correlate (Greve et al. 2005; Solomon & Vanden Bout 2005; see also Section 4), this could suggest that GN20.2a does account for most of the submillimeter emission of GN20.2 from P06, and that GN20.2b could contribute at most some 30% of it but likely not much more. A final argument is that GN20.2 was originally discovered by Chapman et al. (2001) in *photometry* mode with SCUBA at JCMT, pointing at the position of the GN20.2a radio galaxy. This resulted in a submillimeter flux density of $S(850 \mu\text{m}) = 10.2 \pm 2.7$ that is fully consistent with the flux in the P06 map. GN20.2b is $6''.8$ away from GN20.2a and any emission from its position would have been close to the edge of the telescope primary beam, resulting attenuated by a factor of 2. Nevertheless, the Chapman et al. (2001) flux is actually slightly brighter than the flux in P06, although consistent within the errors. Accounting for the errors in the P06 and Chapman et al. (2001) $850 \mu\text{m}$ flux density measurements, this suggests that GN20.2a does contribute at least half of the flux of GN20.2, and possibly most of it.

For completeness, we note that an additional faint radio-detected galaxy is present just $1''$ north outside the edge of the SCUBA beam. This galaxy is a hard X-ray source in the catalog of Alexander et al. (2003), for which we derive a photometric redshift of $z_{\text{phot}} = 1.6$. The radio and mid-IR emission of this object, if entirely due to star formation, would correspond to about $100 M_{\odot} \text{ yr}^{-1}$. This in turn would produce a submillimeter flux of order of 1 mJy or less at $850 \mu\text{m}$. At $8''$ from the P06 position and at $14''$ from the Chapman et al. (2001) pointed observations, any potential submillimeter emission from this

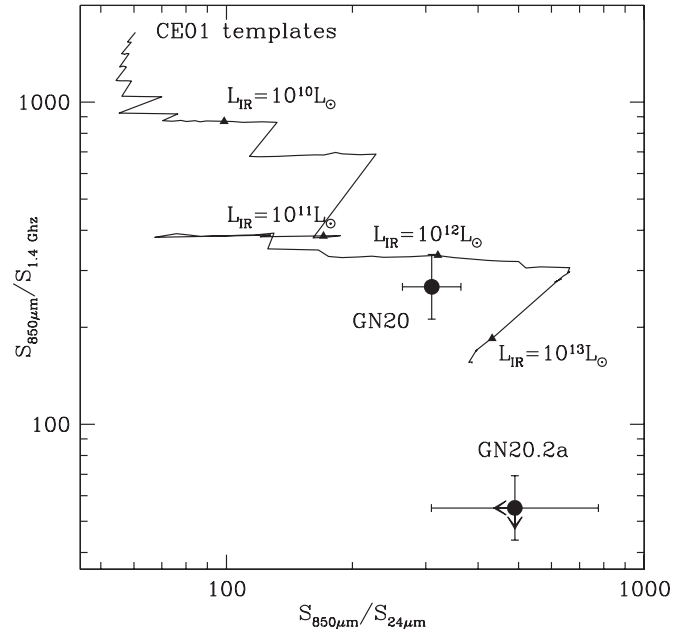


Figure 10. $850 \mu\text{m}$ to $24 \mu\text{m}$ and 1.4 GHz flux density ratios for GN20 and GN20.2a, plotted as filled circles. We assign to GN20.2a the full $850 \mu\text{m}$ flux density of GN20.2 although GN20.2b might be contributing some of the submillimeter flux, as discussed in Section 3.3. In that case, both flux density ratios should be taken as upper limits. The lines show the predicted ratios labeled as a function of bolometric luminosity (L_{IR}) for the CE01 library of templates at a redshift of $z = 4.055$.

galaxy would be negligible for the GN20.2 system $850 \mu\text{m}$ photometry.

In conclusion, our results suggest a scenario in which two $z \sim 4.05$ counterparts might be contributing to the submillimeter emission of GN20.2, although GN20.2a is likely to be the dominant component.

4. THE PHYSICAL PROPERTIES OF $Z = 4.05$ SMGS

4.1. Bolometric IR luminosities

Following the analysis described in Section 3.1.2, the radio-IR SED of GN20 is best reproduced with a CE01 library template corresponding to a luminosity of $L_{\text{IR}} = 3.5 \times 10^{13} L_{\odot}$, redshifted to $z = 4.055$. However, the CE01 library implies a correlation between dust temperature and luminosity that is calibrated on observations in the local universe but that might not necessarily hold at higher redshifts. In order to explore the uncertainties in the determination of GN20's total IR luminosity due to possible SED temperature variations, we again used the CE01 library, but allowing this time for a free normalization of the templates when comparing to the observed fluxes, thus spanning the full range of dust temperatures in the library. For this exercise, we used the measurements or upper limits at $24 \mu\text{m}$, $850 \mu\text{m}$, 3.3 mm , and 20 cm and also included the 1.1 mm and 1.2 mm measurements from Perera et al (2008) and Greve et al. (2008), and the $70 \mu\text{m}$ upper limit from Frayer et al. (2006). Integrating over the best-fitting template yields in this way $L_{\text{IR}} = 2.4 \times 10^{13} L_{\odot}$ and a formal uncertainty (1σ) from the fit of less than 0.05 dex (the luminosity step in the CE01 library). The best-fitting template has an intrinsic $L_{\text{IR}} = 1.5 \times 10^{12} L_{\odot}$ and is scaled up in luminosity by a factor of 16. This would correspond to an SED temperature of about 57 K, lower than those of CE01 templates of comparable luminosities $L_{\text{IR}} \gtrsim 10^{13} L_{\odot}$. The same effect can be appreciated

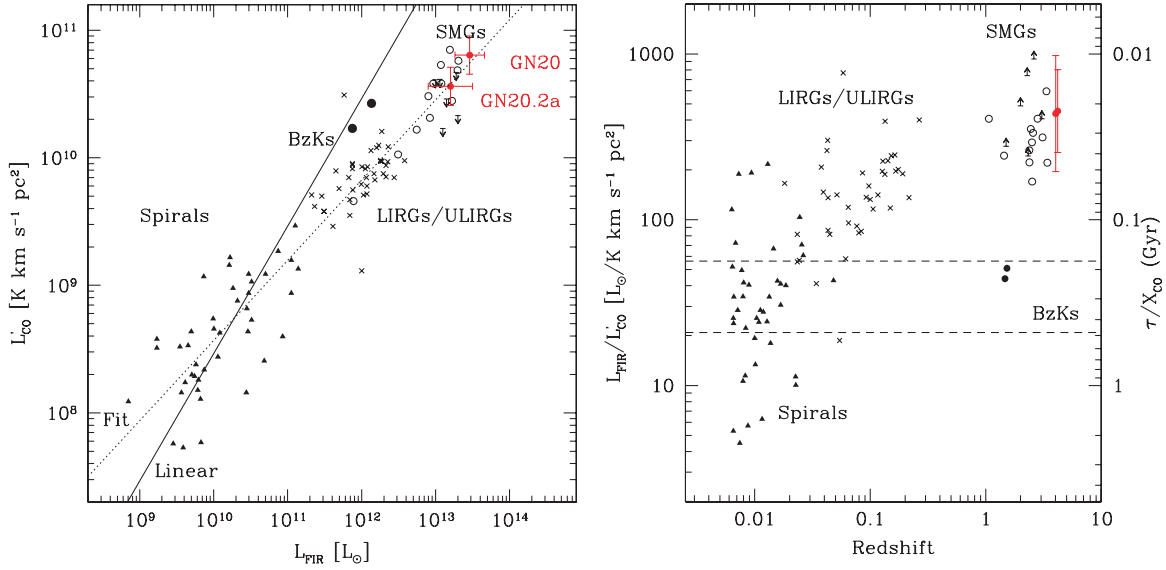


Figure 11. Comparison of FIR to CO luminosities for a variety of local and distant galaxies (see Solomon & Vanden Bout 2005; Greve et al. 2005; figure adapted from Daddi et al. 2008) and the GN20 and GN20.2a galaxies (points with error bars). The FIR estimates for GN20 and GN20.2a are described in the text, based on the radio–IR SEDs. The CO luminosities are estimated from the CO[4–3] transitions for GN20 and GN20.2a, and for a variety of other transitions for the other sources. We assume constant brightness temperature in the various CO transitions for this comparison. Note that CO luminosities (and therefore gas masses) could be underestimated if the observed CO transitions are not thermalized.

(A color version of this figure is available in the online journal.)

more directly in Figure 10 where we show the $850\,\mu\text{m}$ to $24\,\mu\text{m}$ and radio flux density ratios. The GN20 flux density ratios are reasonably in line with CE01 predictions, although the $850\,\mu\text{m}$ to radio flux density ratio is 80% higher than expected for the $L_{\text{IR}} = 10^{13.5} L_{\odot}$ galaxy in the CE01 library. The effect is significant at the 2σ level only, but indeed its SED is closer to the expected ratio for $L_{\text{IR}} = 10^{12} L_{\odot}$ expected ratio. SMGs have been generally found to be somewhat colder than CE01 models, as a result of the selection at $850\,\mu\text{m}$ (P06), so this result is not too surprising.

As a third estimate of the IR luminosity of GN20 we might use directly the radio–IR correlation. The other two estimates also used this correlation to fit the radio, although this was weighted together with all the other measurements. For its measured 1.4 GHz flux density of $75.8\,\mu\text{Jy}$, assuming a radio continuum ($f_{\nu} \propto \nu^{-\alpha}$) with $\alpha = 0.8$, we would derive $L_{\text{IR}} = 2.8 \times 10^{13} L_{\odot}$. It is not obvious which of the three estimates is more reliable but fortunately the measurements are very close, all within a range of less than 0.2 dex. In summary, we adopt the average value of $L_{\text{IR}} = 2.9 \times 10^{13} L_{\odot}$ for our best estimate and an uncertainty of 0.2 dex.

The $850\,\mu\text{m}$ to VLA radio flux density ratio for GN20.2a is about 5 times lower than that for GN20 (Figure 10), implying a strong radio excess of a factor of 4–5. GN20.2a has a radio luminosity of $2 \times 10^{25} \text{ W Hz}^{-1}$ at 1.4 GHz rest frame, again assuming a radio continuum index $\alpha = 0.8$. This demonstrates that a powerful radio-loud AGN is hidden in this $z = 4.05$ source. Therefore, we cannot use the 1.4 GHz flux density to estimate its total IR luminosity. We used the CE01 library templates, with and without allowing for a free normalization, to fit the $24\,\mu\text{m}$, $70\,\mu\text{m}$, $850\,\mu\text{m}$, and 3.3 mm measurements or upper limits. Similarly to GN20, we find $L_{\text{IR}} = 2.2 \times 10^{13} L_{\odot}$ and $L_{\text{IR}} = 1.0 \times 10^{13} L_{\odot}$, the latter being the “free-normalization” case that also prefers a lower temperature template. These estimates use the full $850\,\mu\text{m}$ flux density measurements although some part of this might be due to GN20.2b. This also assumes that the AGN inside GN20.2a is not contributing substantially to the measured $24\,\mu\text{m}$ and

$850\,\mu\text{m}$ flux densities. Pope et al. 2008 showed that this is generally the case for $z \sim 2\text{--}3$ SMGs. Given the uncertainties, we adopt the average of these two estimates, $L_{\text{IR}} = 1.6 \times 10^{13} L_{\odot}$, and an uncertainty of about 0.3 dex.

This analysis implies that GN20 and GN20.2 are extremely luminous galaxies, with $L_{\text{IR}} > 10^{13} L_{\odot}$. Besides being among the most distant known SMGs, these are also some of the most luminous galaxies known so far. We use a Kennicutt et al. (1998) conversion of $\text{SFR}[M_{\odot} \text{ yr}^{-1}] = L_{\text{IR}}[L_{\odot}]/10^{10}$, expressed for the Chabrier 2003 IMF adopted in this paper. The IR luminosities correspond to an SFR of $> 1000 M_{\odot} \text{ yr}^{-1}$ if the IR emission is dominated by star formation. We note that neither the GN20 nor GN20.2a (or GN20.2b) counterparts are detected in the X-rays in the catalog of Alexander et al. (2003), although the radio emission does suggest the presence of an AGN inside GN20.2a. There is no clear evidence, instead, for the presence of an AGN inside GN20. If a top-heavy IMF is adopted, the implied SFR could also become significantly smaller.

4.2. CO Luminosities and Molecular Gas Masses

The observed CO[4–3] fluxes convert to luminosities of $L'_{\text{CO}[4-3]} = 6.2 \times 10^{10} L_{\odot}$ and $L'_{\text{CO}[4-3]} = 3.7 \times 10^{10} L_{\odot}$, for GN20 and GN20.2, respectively. Figure 11 shows that these galaxies appear to lie close to the (nonlinear) correlation between L'_{CO} and L_{IR} traced by local ULIRGs and distant SMGs. Under the assumption that the CO[1–0] and CO[4–3] transitions correspond to the same brightness temperature and assuming $X_{\text{CO}} = 0.8 M_{\odot} (\text{K km s}^{-1} \text{ pc}^2)^{-1}$ (Downes & Solomon 1998; Solomon & Vanden Bout 2005), the CO luminosities convert to total molecular gas masses of $5 \times 10^{10} M_{\odot}$ and $3 \times 10^{10} M_{\odot}$ for GN20 and GN20.2a, respectively. These might be regarded as lower limits if the CO[4–3] transitions observed were not thermalized, the total CO luminosities and gas masses would be higher. VLA observations of CO[1–0] will be able to address this point.

At the observed SFR levels, the gas reservoirs would be exhausted in roughly 20–30 Myr (Figure 11). Similar timescales

have been derived for $z \sim 2\text{--}3$ SMGs by Greve et al. (2005).

4.3. Dynamical and Stellar Mass Estimates

The CO[4–3] emission from GN20 has an FWHM of $710 \pm 120 \text{ km s}^{-1}$, matching well to the typical value of CO-detected SMGs at lower redshifts (Greve et al. 2005). From the higher-resolution B configuration PdBI data alone we find that the CO line is marginally resolved spatially, with an FWHM of $0''.42 \pm 0''.18$ from Gaussian fitting of the uv visibilities performed within GILDAS. The possible extension of the source is supported by the fact that for point source extractions the flux measured with the D-configuration data is higher than the one from the B-configuration data, a 2σ effect suggesting that the CO emission is starting to be resolved at the $1''.3$ resolution of our B-configuration data. This size matches well to the typical CO sizes of $r_e \sim 2 \text{ kpc}$ for SMGs (Tacconi et al. 2006, 2008), and is roughly consistent with its UV extent as well (Figure 5). Recently, Younger et al. (2008b) measured a size of $0''.6 \pm 0''.15$ for GN20 (Gaussian fitting), from the far-IR dust continuum emission at $890 \mu\text{m}$ with the SMA, which is fully consistent with our CO size estimate. The velocity and size correspond to a total dynamical mass of $\sim 2.3 \times 10^{11} \sin i^{-2} M_\odot$ including gas, stars, and dark matter.

Given the molecular gas mass estimates, this corresponds to a molecular gas fraction of about 20%, similar to what is typically found for lower redshift SMGs (Greve et al. 2005). The stellar mass derived from SED fitting of the ACS to IRAC photometry is $\sim 2.3 \times 10^{11} M_\odot$, expressed for a Chabrier (2003) IMF (see e.g., Maraston et al. 2006 for more details on the range of models and assumptions implied). The combined molecular gas and stellar masses, only roughly half of which presumably fall within r_e , add up to roughly 70%–80% of the estimated dynamical mass, close enough within the large uncertainties of such estimates. This implies that the stellar mass is not highly overestimated for the choice of a Chabrier (2003) IMF and the case of a top-heavy IMF is disfavored by the data.

For GN20.2a, using a similar method we infer a stellar mass of $\sim 0.5 \times 10^{11} M_\odot$.

4.4. On the Possibility of Lensing

The intrinsic SFRs and luminosities of these sources might be lower if there is amplification by gravitational lensing (see Paciga & Scott 2009). Lensing by foreground structure could be an alternative way to interpret the fact that colder SEDs, typical of lower luminosity galaxies in the local universe, seem to reproduce better colors of the GN20 and GN20.2 galaxies. In that case, the luminosity would also match those of colder galaxies without the need to advocate evolution in the temperature–luminosity relation of starburst galaxies. However, some evidence against lensing is provided by the FIR to CO properties of GN20 and GN20.2 (Figure 11). If lensed by a factor of 10 or more, the de-lensed properties would place them in a region of the diagram corresponding to a very high star formation efficiency, not commonly observed for $L_{\text{IR}} \sim 10^{12} L_\odot$ sources at high or low redshifts. Following the analysis discussed in Tacconi et al. (2008), the agreement between the dynamical mass estimate and the stellar and gas mass estimates also disfavors the possibility that GN20 is lensed by a very large factor, given that emission line FWHMs should be independent of magnification. Qualitatively, the same picture

also holds for GN20.2a, for which the data suggest a CO[4–3] line FWHM $\sim 1000 \text{ km s}^{-1}$ (albeit with a large uncertainty), not uncommon amongst SMGs (Greve et al. 2005).

4.5. The Relation between Stellar Mass and SFR at $z \sim 4$

A tight correlation exists between the SFR and stellar mass of star-forming galaxies from $z = 0$ to $z \sim 2$, after excluding the locus of quiescent/passive galaxies (Elbaz et al. 2007; Daddi et al. 2007a; Noeske et al. 2007). The implication of this correlation remains subject to debate but suggests that, on average, the processes regulating the star formation activity of a galaxy are the same over a large range of stellar masses. Outliers do exist at both extremes in this correlation. On the low SFR side, the cloud of red-dead galaxies have SFRs lower than expected by several orders of magnitudes. On the high SFR side, ULIRGs and $z \sim 2\text{--}3$ SMGs exhibit approximately 1 order of magnitude larger SFRs for their stellar mass than the average galaxy of equivalent stellar mass (Daddi et al. 2007a; Elbaz et al. 2007). Here, following Daddi et al. 2007a, we use the Tacconi et al. 2008 estimate of SSFR for $z = 2\text{--}3$ SMGs that is based on dynamical masses, which should more robustly represent the total galaxy mass than is possible from stellar mass estimates. We converted the average $L_{\text{IR}} = 10^{13.1} L_\odot$ of the sample into $\text{SFR} \sim 1200 M_\odot \text{ yr}^{-1}$. Takagi et al. (2008) confirm higher SSFRs in SMGs, with respect to normal galaxies of the same masses, using stellar mass estimates, although they find SSFRs that are only a factor of 3 higher on average than those of the ordinary BzK galaxies, with more overlap between samples (see also Dannerbauer et al. 2006 for overlapping objects between the BzK and SMG samples). Their SFRs are based on the radio fluxes and assume a radio–IR correlation with a different normalization respect to the local one by a factor of about 2.

On the low side, the red-dead galaxies appear to fall short of SFR because of a lack of molecular gas fuel, possibly due to negative feedback. However, the excess SFR of $z \sim 2\text{--}3$ SMGs remains to be understood. A possible explanation is external triggering, e.g., by major mergers (Tacconi et al. 2006; 2008) as is seen for local ULIRGs.

When compared to their closer $z \sim 2\text{--}3$ siblings, $z \sim 4$ SMGs appear to be forming stars with an equivalently high SSFR. However, the stellar mass–SFR relation shows a continuous increase of SSFR with increasing redshift from $z = 0$ to 2, which is expected due to the higher gas mass fractions at higher redshifts. The question therefore arises as to whether an SMG could represent the typical star-forming galaxy at $z \sim 4$, unlike their $z \sim 2$ siblings which are atypical compared to the average galaxy at their cosmic epoch (see Figure 12).

In order to address this question, one needs to identify the locus of average star-forming galaxies at $z \sim 4$ and then compare it to the locus of $z \sim 4$ SMGs. We consider the subsample of B -band dropout Lyman break galaxies in GOODS-N with IRAC magnitudes at 5.8 and $8.0 \mu\text{m}$ brighter than 24. The requirement of an IRAC detection is necessary to reliably estimate the stellar masses. The use of B -band dropouts ensures that we are concentrating on star-forming galaxies, with a negligible contribution from passive galaxies. Within this limit, about 10% of the B -band dropouts to $z_{\text{AB}} < 27$ are selected, or 77 sources. We fitted the ACS to IRAC SEDs of these B -band dropouts using Maraston (2005) models with constant star formation, allowing the redshift to vary freely within $3.1 < z < 4.4$ (the 95% confidence region expected for the redshift distribution of B -band dropouts) and also allowing for dust reddening following a Calzetti et al. (2000) law. In

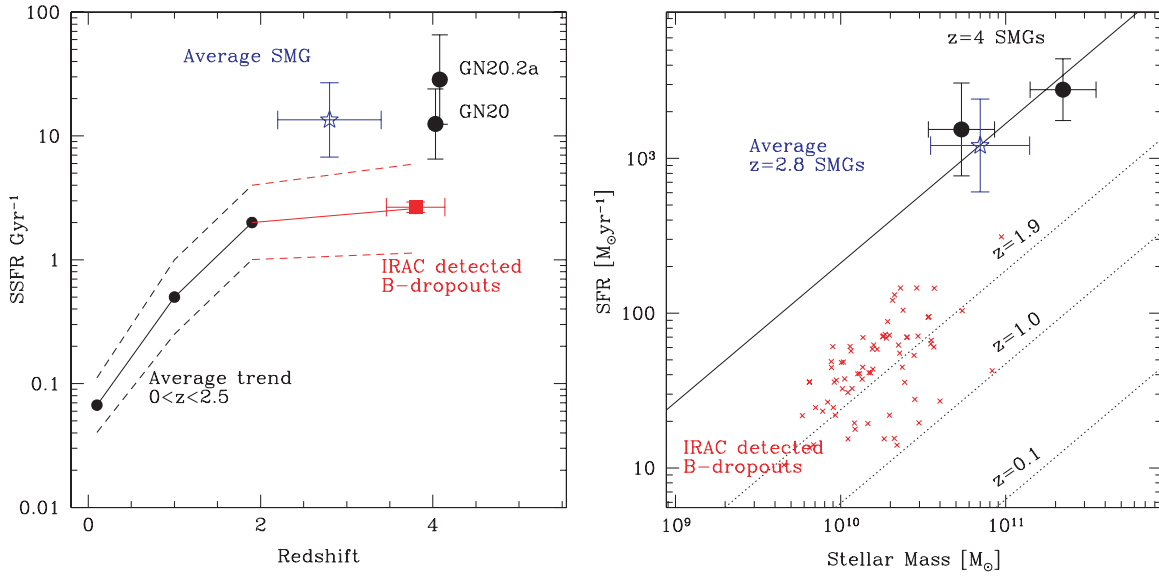


Figure 12. SSFR (SFR to stellar mass ratio) as a function of redshift is shown in the left panel. The right panel shows the stellar mass vs. SFR. Large solid circles are GN20 and GN20.2a. Their stellar masses were derived through SED fitting, and typical errors are found to be of the order of 0.2 dex. The filled square (left panel) and small crosses (right panel) refer to measurements derived for the IRAC detected, massive *B*-band dropout Lyman break galaxies. Stellar masses and SFRs of the *B*-band dropouts were obtained through fitting of the UV to IRAC SEDs. Individual measurements are shown in the right panel, while the left panel shows *B*-dropout's average quantities with error bars showing the error in the mean of the SSFR of the ensemble and the expected range in redshift. Stacking at 850 μm and 1.4 GHz yields upper limits on the average SFR of the order of $55 M_{\odot} \text{ yr}^{-1}$ for the *B*-band dropouts, consistent with the average UV measurements. The star refers to the average of SMGs at $z \sim 2\text{--}3$ from Tacconi et al. (2006); error bars refer to the spread of properties in the sample. Filled black circles in the left panel show the average SSFR vs. redshift at a stellar mass of $5 \times 10^{10} M_{\odot}$ from Daddi et al. (2007a) and Elbaz et al. (2007). The dashed lines show the measured 1σ range (about 0.2 dex at $z = 0.1$ and about 0.3 dex at $z = 1$, and 1.9 and 0.36 dex at $z = 3.8$). We recall that stellar masses and SFRs in this figure are shown for the Chabrier (2003) IMF.

(A color version of this figure is available in the online journal.)

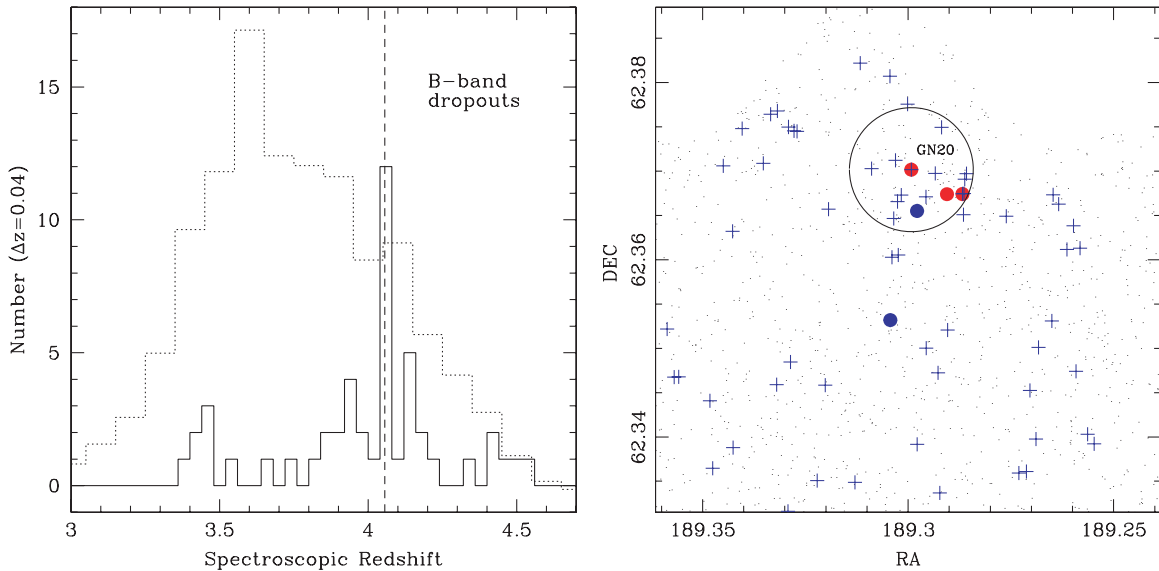


Figure 13. Left panel: spectroscopic redshift distribution of GOODS-N *B*-band dropout Lyman break galaxies, in bins of 0.04 (solid histogram). A strong spike is seen, coincident with the redshift of GN20 and GN20.2a (vertical dashed line). The dotted histogram shows the expected redshift distribution of *B*-band dropouts, based on the simulations of Giavalisco et al. (2004b) and Lee et al. (2006). Right panel: spatial distribution in the northern corner of the GOODS-N field (about $3.5' \times 3.5'$) of $z_{\text{AB}} < 27$ galaxies (small points), and *B*-band dropouts (crosses). The filled symbols are GN20, GN20.2a, and GN20.2b. The large circle shows a $25''$ (180 kpc) radius area centered on GN20. The blue filled symbols are two spectroscopically confirmed galaxies at $z = 4.058$ (closer; this is BD29079, also shown in Figure 5) and $z = 4.047$ (further).

(A color version of this figure is available in the online journal.)

this way, we estimated stellar masses and (basically UV-driven) SFRs for each of the *B*-band dropout Lyman break galaxies. Typical uncertainties from the fit amount to factors of about 2 for both quantities. From this we derive an average stellar mass of $1.5 \times 10^{10} M_{\odot}$ and an average SFR of $40 M_{\odot} \text{ yr}^{-1}$. We performed stacking at 850 μm using the SCUBA supermap of Pope et al. (2005) and with a similar technique to that used

in Daddi et al. (2005b, 2007a). We do not detect the galaxies, deriving a 3σ flux density limit of 0.54 mJy, corresponding to $57 M_{\odot} \text{ yr}^{-1}$. From radio stacking, again performed with a similar technique to Daddi et al. (2005b, 2007a), we get a tentative detection with a peak flux of $1.7 \pm 0.6 \mu\text{Jy}$. The 3σ radio upper limit corresponds to an SFR of $54 M_{\odot} \text{ yr}^{-1}$, consistent with the limit from submillimeter stacking. Overall, the stacking limits

appear to be consistent with the SFRs derived from SED fitting in these galaxies. This is similar to what found at $z \sim 2$ where analogous estimates based on the UV luminosity of galaxies appear to agree well on average with mid- and far-IR estimates (Daddi et al. 2007a).

The locus of typical, massive $z \sim 4$ B -band dropouts does not support a continuous increase of SSFR with redshift, suggesting instead a plateau of the SSFR for $z \gtrsim 2$. The average SFR of $40 M_{\odot} \text{ yr}^{-1}$ places these “typical” $z \sim 4$ galaxies fairly close to the $z \sim 2$ correlation.

The B -band dropout Lyman break galaxies exhibit an average stellar mass lower than that of the $z \sim 4$ SMGs. This implies that not only do $z \sim 4$ SMGs have similar SSFRs to those of their $z \sim 2$ siblings, but they are also found to be outliers with respect to the average star-forming galaxy at their epoch. Note that the similarity of $z = 2$ – 3 and $z = 4$ SMGs is also supported by their equivalently large FIR to CO ratios, corresponding to high star formation efficiencies and rapid gas consumption timescales.

We hypothesize that this favors a triggering mechanism for the activity of the $z \sim 4$ SMGs, such as major mergers. Indeed, GN20.2a has a very nearby ($0''.5$ or 3.5 proper kpc at $z = 4.05$) B -band dropout companion (Figure 5). GN20 has a clumpy morphology that could be reminiscent of a merger (although, see Bournaud et al. 2008). The $0''.5$ offset between the optical light peak and submillimeter/radio and CO position might also point to a complex geometrical situation often found among mergers (e.g., the Antennae; Wang et al. 2004). The high gas densities of a merging event could also explain why, contrary to what is found for typical massive galaxies at $1.4 < z < 2.5$ (Daddi et al. 2007a; Dannerbauer et al. 2006), the emitting region is completely opaque in the UV, similar to $z \sim 2$ – 3 SMGs. Indeed, we find that the radio–IR-based SFR estimates of the $z \sim 4$ SMGs are a factor of > 10 times larger than the UV-based ones.

5. A $Z = 4.05$ PROTO CLUSTER OF GALAXIES IN GOODS-N CENTERED AROUND GN20 AND GN20.2

Down to the limits of the GOODS-N observations of P06, the surface density of SMGs is $\approx 1000 \text{ deg}^{-2}$, and thus the fact that GN20 and GN20.2 are both at $z \sim 4.05$ and are only $24''$ apart, with a projected spatial distance of 169 physical kpc, implies that these two SMGs are spatially clustered (see also Blain et al. 2004). This suggests that these SMGs might also be part of some type of larger, high-redshift structure in GOODS-N.

To investigate further this possibility, we have analyzed the distribution of spectroscopically confirmed Lyman-break galaxies at $z \sim 4$ (B -band dropouts) in GOODS-N (Figure 13; D. Stern et al. 2009, in preparation). We compare the observed redshift distribution to the expected distribution function derived from simulations (Giavalisco et al. 2004b; Lee et al. 2006). There are 12 redshifts in the $\Delta z = 0.04$ bin that includes GN20 ($z = 4.055$); these galaxies define a clear spike in the redshift distribution. There currently are 58 high-quality spectroscopic redshifts of B -band dropouts in the GOODS-N sample distributed over the range $3.5 < z < 4.5$, 12 of which belong to the spike. This is a very strong concentration of galaxies, comparable, for example, to that discovered at $z \sim 3.09$ by Steidel et al. (1998), and it seems unlikely that it can be the result of random (Poisson) sampling. We have generated a large (10^6) ensemble of random realizations of GOODS B -band dropouts of the same size as the observed one using the expected redshift distribution function, and have counted how often a

spike as large as the observed one is realized. In principle, one should also take into account the clustering of B -band dropouts in this simulation; in practice, however, the spatial correlation length, $r_0 \sim 4$ comoving Mpc, of these sources (Lee et al. 2006) is $7\times$ smaller than the radial distance covered by the redshift bin that we have adopted, $\Delta r = 29$ comoving Mpc, implying that over these scales the spatial distribution of the galaxies can be approximated as Poisson.

We found no realization in which the number of galaxies in the redshift bin of GN20 equals or exceeds that of the observed spike, meaning that the probability to get a similar overdensity by chance is less than 10^{-6} . The simulations show that the average number of galaxies in the 0.04 redshift bin is 1.31 ± 1.18 , implying that the observed spike corresponds to an overdensity of a factor of 8.4 and is significant at the 8.2σ level. These redshift concentrations are frequently found among Lyman-break galaxies at $z \sim 3$. For example, similar concentrations are found in every survey field for U -band dropouts by Steidel et al. (2003). Vanzella et al. (2008) also report evidence of concentrations in the redshift distribution of B -band dropouts in the GOODS-South field.

To gain additional information about the nature of the GN20 structure, especially its transverse size, we have studied the distribution of the angular positions of B -band dropouts in the field and around the GN20 complex. Of the 765 B -band dropouts to $z_{\text{AB}} < 27$ in GOODS-N, counting all sources regardless of a spectroscopic identification, 14 are within $25''$ from GN20 (2.5 Mpc^2 comoving; see Figure 14). This is an overdensity of a factor of 5.4, the strongest concentration of B -band dropout Lyman break galaxies found in GOODS-N. Given that at these angular scales the angular correlation function of B -band dropouts is non-negligible (Lee et al. 2006), we account for the variance due to clustering to derive an expected rms fluctuation in the counts within $25''$ radius apertures of about 1.8 galaxies. Therefore, the excess counts that we see in the $25''$ radius region surrounding GN20 correspond to a 5.8σ fluctuation. Taken together with the analysis of the redshift spike, this leads us to conclude that the GN20–GN20.2 SMG pair is part of a very strong overdensity with a size consistent with that of a cluster of galaxies, most likely a protocluster given the redshift.

Additional evidence for the presence of a strong overdensity in this structure comes from Mancini et al. (2009), who use photometric redshifts to identify galaxy candidates at $z > 3.5$ from an IRAC sample limited to $m_{4.5\mu\text{m}} < 23$. They find a total of 54 candidates in their full GOODS-N IRAC catalogs, which covers 180 arcmin^2 . Of these massive galaxies, four are within $25''$ from GN20 (GN20 itself, GN20.2a, GN20.2b, and BD29079; all are shown in Figure 5). This corresponds to an overdensity of a factor of 18 for this IRAC-selected sample, with a chance probability of $\sim 10^{-4}$ assuming no spatial clustering (Poisson statistics; 0.16 galaxies expected on average and three observed in addition to GN20).

The possibility that we have uncovered a protocluster is reinforced by the fact that a number of massive galaxies appear to be part of this structure. With an estimated total baryonic mass of $\sim (2\text{--}3) \times 10^{11} M_{\odot}$, GN20 is likely one of the most massive galaxies in this structure. The presence of more than a dozen additional B -band dropouts in this 2 Mpc^2 spatial concentration implies a total baryonic mass reaching $\sim 10^{12} M_{\odot}$ for the overdensity. If we assume the typical mass-to-light ratio of ~ 50 for local massive clusters (Lin et al. 2003), this suggests

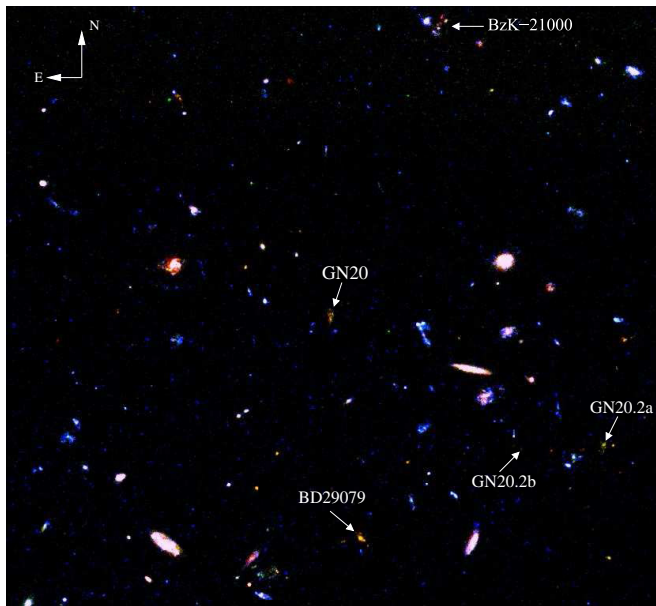


Figure 14. *HST*+*ACS* color image of the field around GN20, derived from F435W (blue), F775W (green), and F850LP (red). The image size is $50''$, or 1.77 comoving Mpc at $z = 4.05$. Close-ups of GN20, GN20.2a, GN20.2b, and the luminous B-dropout galaxy BD29079 are shown in Figure 5. The BzK-21000 galaxy at the top of the image was the original target of the PdBI observations (Daddi et al. 2008). Additional dropouts in the field can easily be recognized from their yellow colors (e.g., see Figure 12).

(A color version of this figure is available in the online journal.)

a lower limit to the total (dark) mass of the protocluster of about $5 \times 10^{13} M_{\odot}$.

These lines of evidence all support the identification of a large structure at redshift $z \sim 4$. While its transverse size appears to be around 2 Mpc (comoving) in diameter, its radial size remains basically unconstrained given that the errors on the redshift measurements are already comparable to the transverse size, not even considering peculiar motions along the radial direction. In addition, a significant overdensity at $z = 4.05$ seems to be present extending over the whole GOODS-N field. This suggests that we are witnessing a protocluster of galaxies which, considering the incompleteness in all the samples we have been discussing, encompasses a total mass of $\approx 10^{14} M_{\odot}$.

It is interesting to compare the GN20 environment with other structures previously discovered at high redshift around powerful steep-spectrum radio galaxies (Kurk et al. 2000; Venemans et al. 2002, 2007; Miley & de Breuck 2008, and references therein). The most direct parallel is with the protocluster around TN J1338-1942 (De Breuck et al. 1999; Venemans et al. 2002) at $z = 4.1$. A study of the overdensity of *B*-band dropout galaxies around this source has been performed by Miley et al. (2004), reporting factors of 2.5–5 excess of Lyman break galaxies (significant at the 3σ – 5σ) level, depending on the spatial scale. This is fairly similar to what is found here for the overdensity around GN20. The field around TN J1338-1942 was also observed at 1.2 mm by de Breuck et al. (2004), who found an overdensity at millimeter wavelengths as well, although without spectroscopic confirmations so far.

Also, it is interesting to note that, contrary to the structure described by Chapman et al. (2009) at $z = 1.99$, where five SMGs are found but without a strong overdensity of UV-selected galaxies, in this case the two SMGs that we have found at $z = 4.05$ (and more SMGs might well be at $z = 4.05$ in the

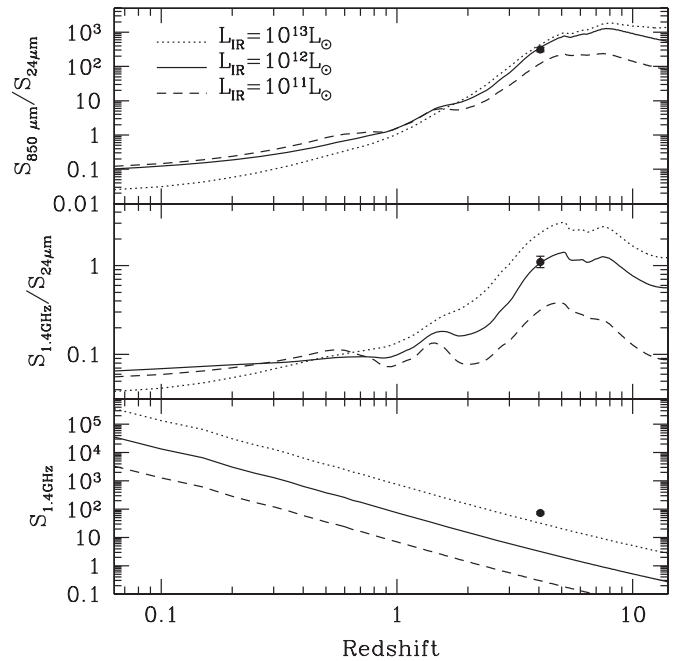


Figure 15. Redshift dependences of several flux density ratios and the 1.4 GHz radio flux density expected for CE01 models with $L_{\text{IR}} = 10^{11} L_{\odot}$ (dashed line), $L_{\text{IR}} = 10^{12} L_{\odot}$ (solid line) and $L_{\text{IR}} = 10^{13} L_{\odot}$ (dotted line). The filled symbols show the values for GN20, which would be detectable up to $z \sim 8$ to the 5σ limits of $20 \mu\text{Jy}$ in our 1.4 GHz map in GOODS-N (G. Morrison et al. 2009, in preparation).

GOODS-N field, see Section 6) do appear to coincide with a strong overdensity of Lyman break galaxies as well.

6. RADIO-IR PHOTOMETRIC REDSHIFTS FOR SMGS

An important result of this paper is the success in identifying the $z \sim 4$ redshifts for the GN20 and GN20.2 galaxies based only on the flux measurements at $24 \mu\text{m}$, $850 \mu\text{m}$, and 20 cm. The ratio of 20 cm to $850 \mu\text{m}$ flux density is, alone, a powerful redshift indicator for dusty SMGs (Carilli & Yun 1999, 2000),¹⁴ although limited in its application by its strong dependence on SED temperature. Clearly, colder galaxies (P06) are intrinsically brighter at $850 \mu\text{m}$ at fixed radio flux density and redshift (e.g., P06). In our approach, however, we have exploited the $24 \mu\text{m}$ measurement that lies on the opposite side of the SED peak. It turns out that for the variations in the shape of local SEDs (as codified in the CE01 library) the $850 \mu\text{m}$ to $24 \mu\text{m}$ flux density ratio is fairly constant at fixed redshift, compared to the redshift excursion of its value (Figure 15), e.g., this ratio changes by factors of $\lesssim 2$ at fixed redshift when the bolometric luminosity L_{IR} varies by a factor of 10. However, at fixed L_{IR} this ratio changes by almost 4 orders of magnitude when going from $z = 0.5$ to $z = 5$ (Figure 15). Note that we have not renormalized the CE01 template models when fitting observed data from the GN20 and GN20.2 galaxies (Figure 15; bottom panel). This information is a powerful complement to the flux density ratios, as it helps pinpoint the correct intrinsic source luminosities, thus helping to solve dust temperature degeneracies, assuming that the local correlations between temperature and luminosity

¹⁴ We applied this redshift indicator to the counterparts of the two SMGs presented here. For GN20, we obtain $z = 3.74$. For GN 20.2a, we obtain $z = 1.61$ and for GN 20.2b we obtain $z = 4.04$. The low photometric redshift obtained for GN 20.2a indicates that the radio emission must be contaminated by an AGN, which substantially affects the Carilli & Yun indicator.

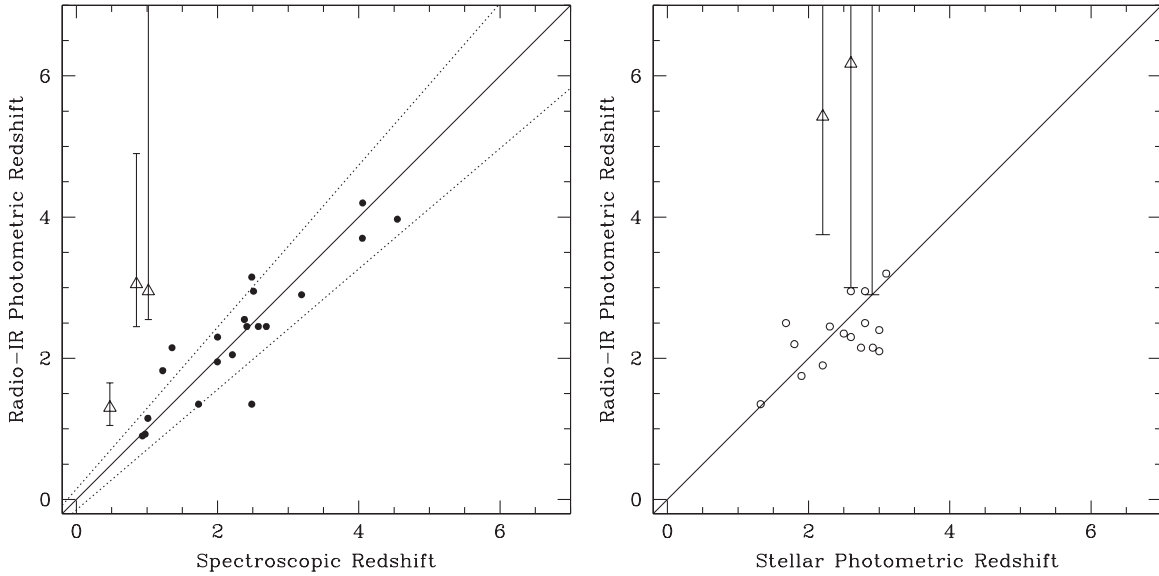


Figure 16. Left panel: radio-IR photometric redshifts for SCUBA counterparts with known spectroscopic redshifts from P06 for GOODS-N and Lehmann et al. (2001), Ivison et al. (2005), Chapman et al. (2005) for Lockman Hole. Empty triangles with error bars (99% levels) are GN13, GN04.2, and GN28 from P06. We suggest that these sources are not the correct counterparts to the submillimeter emission based on the discrepant radio-IR photometric and spectroscopic redshifts. Right panel: the same comparison, but with counterparts having only photometric redshifts determined from the properties of the stellar SED, from P06 and Egami et al. (2004). Triangles with error bars are sources which are consistent with a $z > 4$ solution of the radio-IR photometric redshifts.

measured by CE01 and the radio-FIR correlation are not severely altered in the distant universe. As a result, the photometric redshift estimates based on IR and radio appear to be robust against SED temperature/shape variations, as shown by the case of GN20 and its possibly colder SED (Figures 8 and 10).

Encouraged by the apparent success of this technique, we explored in more detail the possibility of deriving accurate radio-IR photometric redshifts using mid-IR, submillimeter, and radio observations. We applied this technique to the sample of well-studied SMGs in GOODS-N (P06) and the Lockman Hole (Scott et al. 2002; Ivison et al. 2002; Egami et al. 2004), considering only the most likely counterparts. Our radio-IR photometric redshifts are determined as described in Section 3.1.2 for GN20. In particular, in order to effectively use the $850\ \mu\text{m}$ information in the fit, we limit the S/N of the $24\ \mu\text{m}$ and $20\ \text{cm}$ flux density to a maximum of 10, artificially increasing the relative error bars if the S/N is higher. Table 4 summarizes the radio-IR photometric redshift constraints.

The results of this comparison are seen in Figure 16. In the left panel, we show SMGs with counterparts that have measured spectroscopic redshifts. The agreement between radio-IR photometric redshifts and the spectroscopic redshifts is fairly good, with a semi interquartile range of $\Delta z/(1+z) = 0.12$. This figure includes also the Capak et al. (2008) source (assuming a ratio of 2.8 between the $850\ \mu\text{m}$ and $1.2\ \text{mm}$ flux densities), but the result does not change substantially if this one is excluded.

We identify three galaxies where the radio-IR photometric redshifts disagree with the spectroscopic redshifts at more than 99% confidence, suggesting that the proposed optical counterparts to the submillimeter emission may be incorrect. These three galaxies are from the P06 sample, and they are all characterized by having separations $> 6''$ from the SCUBA position. Given that P06 finds a median separation of $\sim 3''$ for secure counterparts, with 80% being at $< 4''.5$,¹⁵ the

large offsets alone suggest that the counterpart identification might have failed for these objects. Only three out of 43 targets are identified as such, and two of these were already listed as tentative counterparts, confirming the high quality of counterpart identification in the original work. We discuss these three objects here in some detail.

1. GN13: the counterpart in P06 is a galaxy at $z_{\text{spec}} = 0.475$ lying $7''$ from the submillimeter position. The identification was judged to be secure, on the basis of the low probability of a chance association between a radio and mid-IR bright source relative to the submillimeter position. Its $850\ \mu\text{m}$ flux density of $1.9\ \text{mJy}$, despite being quite faint intrinsically, is about six times brighter than expected on the basis of both the $24\ \mu\text{m}$ and $20\ \text{cm}$ radio flux densities for its redshift, assuming the CE01 templates. We inspected the other galaxies present in the submillimeter beam, and found no other convincing counterpart. This SMG could be at quite high redshift.
2. GN04.2: the counterpart listed by P06 is at $z_{\text{spec}} = 0.851$ and is $5''.7$ from the submillimeter position. The $24\ \mu\text{m}$ and radio flux densities are both too faint to be consistent with the $850\ \mu\text{m}$ flux density of $2.7\ \text{mJy}$ at this redshift, assuming the CE01 templates. Furthermore, this source is no longer detected in the latest and deepest $20\ \text{cm}$ reduction (G. Morrison et al. 2009, in preparation); the P06 results were based on a 3σ detection at $20\ \text{cm}$. No other $24\ \mu\text{m}$ detected galaxy is present in the beam, which may imply that the real counterpart is at fairly high redshift.
3. GN28: the counterpart listed by P06 is at $z_{\text{spec}} = 1.020$ and is $5''.8$ from the submillimeter position. There is a strong inconsistency between the faint $24\ \mu\text{m}$ flux density of this galaxy ($20.5\ \mu\text{Jy}$) and its $850\ \mu\text{m}$ emission ($1.7\ \text{mJy}$). The $850\ \mu\text{m}$ to $24\ \mu\text{m}$ ratio is 2 orders of magnitude larger than expected for star-forming galaxies at $z = 1$ (Figure 15), and would be even more discrepant for an AGN SED. The $20\ \text{cm}$ radio position is close to the radio lobes of a bright radio galaxy at a similar redshift, and thus may be severely

¹⁵ Dannerbauer et al. (2004) also find a median separation of $3''$ for the radio counterparts of MAMBO sources, with a similar percentage of radio counterparts being separated by less than $4''.5$.

Table 4
Radio–IR Photometric Redshifts of SMGs

ID	$z_{\text{stars/CO/PAH}}^{\text{orig}}$	Redshift Type	$z_{\text{radio-IR}}^{\text{best}}$	$z_{\text{radio-IR}}^{\text{min}}$	$z_{\text{radio-IR}}^{\text{max}}$	χ^2
GN01	2.415	2	2.45	2.05	2.65	8.43
GN02	1.32	1	1.35	0.05	2.15	13.65
GN03	2.2	0	1.90	0.05	2.30	7.46
GN04a	2.578	2	2.45	2.00	3.80	0.01
GN04b	...	−1	3.70	2.40	9.35	0.00
GN04.2	0.851	2	3.05	2.45	4.90	0.01
GN05	2.21	2	2.05	1.25	2.35	1.79
GN06	2.00	2	2.30	2.10	2.40	0.48
GN07a	...	−1	3.65	3.35	4.10	25.56
GN07b	1.998	2	1.95	1.35	2.20	18.75
GN09	2.9	0	13.42	2.90	15.50	18.63
GN10	2.2	0	5.43	3.75	11.90	3.02
GN11	2.3	0	2.45	2.20	2.60	17.89
GN12	3.10	1	3.20	2.90	3.50	0.69
GN13	0.475	2	1.30	1.05	1.65	4.15
GN15	2.74	1	2.15	1.90	2.35	23.27
GN16	1.68	1	2.50	2.40	2.60	12.74
GN17	1.73	2	1.35	1.15	1.65	5.98
GN18	2.8	0	2.50	2.25	2.70	1.43
GN19a	2.484	3	3.15	2.70	6.00	0.50
GN19b	2.484	3	1.35	0.05	2.10	5.23
GN20	4.055	3	4.20	3.45	4.80	17.59
GN20.2a	4.051	3	3.70	3.35	4.05	21.27
GN21	2.8	0	2.95	2.60	3.60	0.25
GN22	2.509	2	2.95	2.60	3.50	1.21
GN23	2.6	0	2.95	2.55	3.35	1.48
GN24	2.91	1	2.15	0.10	2.70	5.16
GN25	1.013	2	1.15	0.35	1.40	1.48
GN26	1.223	3	1.82	1.50	1.95	13.94
GN28	1.020	2	2.95	2.55	14.60	10.38
GN30	1.355	2	2.15	1.45	2.45	0.37
GN31	0.935	2	0.90	0.05	1.30	8.86
GN32	1.9	0	1.75	0.05	2.35	4.84
GN37	3.190	2	2.90	0.10	15.50	1.89
LE850.1	2.60	1	2.30	2.10	2.80	10.65
LE850.4	2.60	1	6.18	3.00	15.50	0.02
LE850.7	1.80	1	2.20	1.95	2.45	1.18
LE850.8b	3.00	1	2.10	1.35	2.55	2.96
LE850.8a	0.974	2	0.93	0.05	6.20	14.83
LE850.14b	2.50	1	2.35	2.05	3.05	0.56
LE850.14a	2.380	2	2.55	1.45	4.35	0.01
LE850.18	2.690	2	2.45	1.95	3.15	0.28
LE850.35	3.00	1	2.40	1.85	2.80	1.11
Capak	4.547	3	3.97	3.00	5.20	0.22

Notes. GN galaxies are from P06. LE850 galaxies are from Egami et al. (2004). The last object is from Capak et al. (2008). “Redshift Type” indicates the origin of stellar photometric redshifts ($z_{\text{stars/CO/PAH}}^{\text{orig}}$): 0 for *Spitzer*+IRAC/MIPS photometric redshifts (P06), 1 for ordinary photometric redshifts from stellar emission, 2 for spectroscopic redshifts (usually optical/UV redshifts or *Spitzer* IRS redshifts derived mainly from detection of PAH features), 3 for CO redshifts. The CO redshifts for GN19a and GN19b are from Tacconi et al. (2008), the one for GN26 is from Frayer et al. (2008), those for GN20 and GN20.2a are from this paper. Some of the P06 photometric redshifts listed in P06 were slightly off; here we list the correct values. New spectroscopic redshifts for three P06 galaxies were measured with IRS in Pope et al. (2008). Ranges in $z_{\text{radio-IR}}$ are given at the 99% confidence level ($\Delta\chi^2 = 6.63$) following Avni (1976) for a single interesting parameter in the fit (e.g., redshift). For the cases of double components, we assigned the total submillimeter flux to each component while computing the photometric redshift. The photometric redshifts listed here for the GN20 and GN20.2a galaxies did not use the 3.3 mm continuum measurements, for consistency with the rest of the galaxies.

contaminated. No other 24 μm detected galaxy is present in the beam, which may also imply that the real counterpart is at fairly high redshift.

When excluding these three likely incorrect counterparts, we find $\sigma(\Delta z/(1+z)) = 0.15$ and a semi-interquartile range of $\Delta z/(1+z) = 0.08$.

The right panel of Figure 16 compares the radio–IR photometric redshifts with independent photometric estimates based largely on the stellar light at optical through IRAC wavelengths (plus the IRAC to MIPS colors in a few cases from P06). Again, the agreement is quite good, with a similar $\sigma(\Delta z/(1+z)) = 0.14$. We find only two cases of widely discrepant estimates, discussed here in some detail.

1. GN10: P06 assign a $z = 2.2$ photometric redshift, while we find $z > 3.7$ at the 99% confidence level, in good agreement with Wang et al. (2007, 2009) and Dannerbauer et al. (2008). The discrepancy is likely due to the photometric redshift of P06 being too low, while the counterpart identification appears correct and agrees with Wang et al. (2007, 2009) and Dannerbauer et al. (2008).
2. GN16: The P06 identification appears correct, and the discrepancy is due to the low photometric redshift ($z_{\text{phot}} = 1.68$) estimate of P06.

We have also applied the radio–IR photometric redshift technique to the CO-detected SMG galaxy reported by Capak et al. (2008) and Schinnerer et al. (2009) to be at $z = 4.547$. The resulting photometric redshift is $z = 4.0$ and the 99% confidence range is $3.0 < z < 5.2$, supporting the $z = 4.5$ redshift identification of this SMG despite the large offset ($\gtrsim 1''$; $\gtrsim 10$ kpc proper) between its Ly α emitting optical counterpart and the radio emission.

In conclusion, we find that radio–IR photometric redshifts can be used as a powerful and independent complement to photometric redshifts derived from stellar emission, and could greatly improve the SMG counterpart identification process. Some differences and evolutionary trends are seen when studying the SEDs of SMGs in detail (e.g., Pope et al. 2006, 2008). However, the fact that direct fitting of locally derived CE01 templates yields reasonable photometric redshifts without any significant bias suggests that ULIRG SEDs have not dramatically evolved from $z = 0$ to $z = 4$.

7. THE SELECTION AND SPACE DENSITY OF THE HIGHEST REDSHIFT STARBURST GALAXIES

We emphasize that not all radio faint (e.g., $S_{1.4\text{GHz}} < 30 \mu\text{Jy}$) counterparts to SMGs are likely to be at $z \gtrsim 4$. For example, four SMGs (GN03, GN11, GN14 (HDF 850-1), and GN18) have even fainter radio flux densities than GN10 and have similar properties to GN10 at other wavelengths, e.g., they are undetected in ACS imaging and have red IRAC SEDs. Dannerbauer et al. (2008) suggest they could lie at $z \gtrsim 4$. In contrast, the radio–IR photometric redshifts suggest that GN03, GN11 and GN18 are at $2 < z < 3$, which is still consistent with their IRAC SEDs. This is because these galaxies have quite bright 24 μm flux densities, much larger than the radio ones. Besides GN20, GN20.2a and GN20.2b, only four other objects from P06 are identified by the photometric redshift technique to have possible radio–IR photometric redshifts $z \gtrsim 4$. With various degrees of confidence, they are GN10, a very solid $z \gtrsim 4$ source also identified by Wang et al. (2007, 2009) and Dannerbauer et al. (2008), and GN13, GN28 and GN04.2, where reliable counterparts are, however lacking, thus making these less convincing candidates. Another well known $z \gtrsim 4$ candidate from GOODS-N is the galaxy HDF850.1 (Dunlop et al. 2004), listed as GN14 in P06, for which we have not

Table 5
Properties of the $z > 3.5$ Starburst Candidates Selected Using their High Radio 1.4 GHz to 24 μm Flux Density Ratios

ID	R.A.(J2000)	Decl.(J2000)	$S_{1.4\text{GHz}}$ (μJy)	$S_{24\mu\text{m}}$ (μJy)	$S_{8.0\mu\text{m}}$ (μJy)	$S_{4.5\mu\text{m}}$ (μJy)
VLA 512	12:36:58.49	62:09:31.8	47.3 ± 11.5	36.8 ± 5.0	9.7 ± 1.0	4.0 ± 0.4
VLA 812	12:35:53.24	62:13:37.5	45.6 ± 5.1	33.0 ± 6.2	23.1 ± 2.3	14.6 ± 1.5
VLA 966	12:37:01.52	62:20:24.6	64.2 ± 5.3	49.7 ± 3.6	22.9 ± 2.3	14.2 ± 1.4

obtained a radio–IR photometric redshift due to the lack of reliable radio and 24 μm data. This would make a total of eight plausible $z > 4$ SMGs in GOODS-N in a total area of roughly 50–100 arcmin² covered with SCUBA (with a highly inhomogeneous coverage; see, e.g., Pope et al. 2005), or roughly 200–300 galaxies deg^{−2}. Using the volume in $3.5 < z < 6$, this corresponds to a space density of $\approx 10^{-5}$ Mpc^{−3}, which compares fairly well with expectations for the very high redshift formation of the oldest early-type galaxies seen at $z \sim 1.5$ – 2.5 (see Section 1). With typical SFRs in excess of $1000 M_{\odot} \text{ yr}^{-1}$, such a population contributes an SFRD of order of $2 \times 10^{-2} M_{\odot} \text{ yr}^{-1} \text{ Mpc}^{-3}$, already comparable to the global contribution of Lyman break galaxies at these redshifts (Giavalisco et al. 2004b).

7.1. A Radio/24 μm Selection Criterion for High- z Starburst Galaxies

For the most reliable $z \gtrsim 4$ starbursts (GN10, GN20, GN20.2a) we note that all of these have very high 20 cm to 24 μm flux density ratios, greater than ~ 1 (Figure 15). GN20.2b itself satisfies such a criterion and might also be at $z = 4.05$. This suggests that a criterion $S_{1.4\text{GHz}} \gtrsim S_{24\mu\text{m}}$ could be useful at singling out the very high redshift tail of SMGs. Applying this criterion to the P06 sample we recover the SMGs listed above, plus GN12, GN16 and GN19a, all sources at $2.5 < z \lesssim 3.2$, a distribution clearly skewed to higher redshifts than typical SMGs. The $z = 4.547$ galaxy from Capak et al. (2008) also satisfies this criterion.

In principle, this simple criterion could be applied regardless of a submillimeter detection, and could avoid the inherent bias toward intrinsically cold sources. Of course, care should be taken and a careful analysis of all multiwavelength information should be performed on targets selected in this way, as radio emission from radio-loud AGNs would bias the radio to 24 μm flux density ratio. Mid-IR emission can also be boosted by AGNs, which could make genuine $z > 4$ objects fail this criterion. More importantly, given the relatively small dynamic range expected over redshift for the 20 cm to 24 μm flux density ratios in galaxies (Figure 15), scatter due to SED variations can imply a substantial contamination from lower redshift sources.

We have performed a preliminary test of this criterion using a sample of radio selected galaxies with $S_{1.4\text{GHz}} > 30 \mu\text{Jy}$ in GOODS-N (G. Morrison et al. 2009, in preparation), applying a simple but very conservative approach. By requiring $S_{1.4\text{GHz}} > 0.8 \times S_{24\mu\text{m}}$, 63 radio sources are retained. Only half of these (34) are undetected in the ACS F435W band ($S/N < 2$), a necessary condition for being at $z \gtrsim 4$. Of these, 16 are also consistent with having a red IRAC SED, with a peak beyond 7 μm , as expected for $z \gtrsim 4$.¹⁶ We further require relatively blue *Spitzer*+MIPS to IRAC flux density ratios: $S_{24\mu\text{m}}/S_{4.5\mu\text{m}} < 13$

and $S_{24\mu\text{m}}/S_{8.0\mu\text{m}} < 5$, as observed in the bona-fide $z \gtrsim 4$ sample (GN20, GN20.2a, GN20.2b, GN10), leaving us with 11 galaxies. This excludes from the sample the $z = 4.424$ radio source from Waddington et al. (1999), where the near-IR to mid-IR spectral range is likely dominated by a powerful AGN. Finally, we exclude all sources detected in the X-ray catalog of Alexander et al. (2003) which, if at $z \gtrsim 4$, must be AGN dominated. This leaves us with seven sources, including the three reliable $z > 4$ galaxies already known (GN20, GN20.2a, GN10) plus GN20.2b. We consider the properties of the three new candidates in detail.

1. VLA 512: this object is undetected in a relatively shallow region of the SCUBA supermap. However, some signal is found at its position with $S_{1.1\text{mm}} = 3.2 \text{ mJy}$ ($S/N = 3.4$) in an AzTEC map of GOODS-N (G. Wilson, private communication). This source has no counterpart at any ACS band, and is a good high-redshift starburst candidate.
2. VLA 812: this galaxy is very close to the edge of the SCUBA supermap, where the noise is fairly high. However, this source is listed in Chapman et al. (2005) as a SCUBA detection in photometry mode ($S_{850\mu\text{m}} = 8.8 \pm 2.1 \text{ mJy}$), with a redshift of $z = 2.098$. The source is also detected by Perera et al. 2008 and Greve et al. 2008 at 1.1 mm and 1.2 mm with MAMBO and AzTEC, respectively. We find that a relatively bright $z = 2.098$ galaxy is present in the area, but 2'' away from the IRAC and radio position, which corresponds instead to a faint galaxy with ACS photometry of $i_{\text{AB}} = 27.6$ and $z_{\text{AB}} = 27.3$, undetected in the B and V bands. We suggest that the Chapman et al. (2005) redshift identification does not correspond to the actual counterpart of the radio and submillimeter emission. This radio source is a reliable candidate for a very high redshift starburst ($z \gtrsim 4$).
3. VLA 966: we place a 3σ upper limit of $S_{850\mu\text{m}} < 8.1 \text{ mJy}$ from the SCUBA supermap at the position of this source. Its optical counterpart is a B -band dropout with ACS magnitude $z_{850} = 26.6$ and red IRAC SED, confirming that this is a reliable $z \sim 4$ candidate. The VLA radio flux density of this source is comparable to that of GN20. The lack of submillimeter emission could signal a warmer SED (see e.g., Chapman et al. 2008).

We note that, due to the very conservative requirements applied, we finally retained only three galaxies of the 63 selected down to 30 μJy in GOODS-N with our radio/24 μm criterion as bona-fide $z \gtrsim 3.5$ starburst galaxy candidates. We believe that we efficiently rejected in this way all contamination from AGN dominated radio galaxies. Several of the discarded galaxies are most likely to be starbursts at $2.5 \lesssim z \lesssim 3.5$, still very interesting objects but beyond the scope of the simple exercise described in this Section where we focus on the $z > 3.5$ redshift tail. We are probably also missing several other genuine $z \gtrsim 3.5$ starbursts due to the very strict requirements that we have applied. For example, we required a distinct photometric peak in IRAC beyond 7 μm , but this can be weak or washed

¹⁶ The Capak et al. (2008) galaxy does not satisfy this requirement. The authors suggest that line emission contaminates the IRAC photometry for this source. A possible alternative is that the IRAC flux is actually from a foreground, lower redshift galaxy. This would imply that the SMG is very faint even at the IRAC bands, perhaps similar to GN10.

out due to the S/N level of the IRAC data. We required X-ray nondetections, but powerful starbursts might also contain an unobscured AGN that does not necessarily affect the radio emission to a significant degree. Given the promising results of this attempt, we will defer to future work an investigation of the properties of the full sample of galaxies selected with this radio/24 μm criterion.

Although we by no means claim to have selected a complete sample, the existence of these three additional $z > 3.5$ starburst candidates reinforces our conclusion that a substantial population of vigorous star-forming galaxies was already present at early epochs.

7.2. Predictions for Future Herschel Surveys

We now consider expectations for forthcoming *Herschel* surveys to detect very high redshift starbursts. *Herschel* will obtain FIR imaging with an unprecedented sensitivity at 70 μm , 100 μm and 160 μm with PACS (Poglitsch et al. 2006) and at 250 μm , 350 μm and 520 μm with SPIRE (Griffin et al. 2007).

We computed the expected flux densities of GN20 in the *Herschel* bands, based on various assumptions. Using the best-fitting $z = 4.055$ unscaled CE01 model shown in Figure 8, we predict flux densities of about 40–50 mJy in the SPIRE bands, 24 mJy at 160 μm , 4.8 mJy at 100 μm and 1.8 mJy at 70 μm . The latter value is comparable, but still consistent, with the *Spitzer* 70 μm upper limit. If these predictions are correct, galaxies similar to GN20 should be very easily detectable with *Herschel*, e.g., over the full 70 deg² survey of the Hermes guaranteed time consortium,¹⁷ which could yield hundreds $z > 4$ hyperluminous infrared galaxies. Even if we used a colder template following Figure 10, normalized conservatively at a 1σ lower 850 μm flux density of 17 mJy, we would still predict flux densities of about 30 mJy at 350 μm and 520 μm , which is still above the expected flux limit of the 70 deg² Hermes survey.

This suggests that, while strongly limited by confusion to quite bright flux densities (~ 15 mJy; Le Borgne et al. 2009), the *Herschel* SPIRE observations will efficiently detect a significant tail of very high redshift ($z > 4$) starbursts. Due to the relation between redshift and 850 μm flux density (Ivison et al. 2002; Pope et al. 2006), *Herschel* might detect the bulk of the most active merger-powered galaxies in the distant universe, possibly accounting for an important fraction of the SFRD in the early universe. Clearly, a real challenge will be to recognize such very high redshift galaxies in the *Herschel*-selected samples, which will require deep multi-wavelength information.

8. SUMMARY AND CONCLUSIONS

The serendipitous detection of CO emission lines at $z > 4$ from deep PdBI observations has allowed a first investigation of the nature and properties of vigorous star-forming galaxies at these redshifts. The main results of this paper can be summarized as follows.

1. CO emission lines are detected at the position of two bright SMGs in the GOODS-N field: GN20 and GN20.2a. A tentative CO signal is seen for an additional radio galaxy in the field, named GN20.2b.
2. We identify the lines of GN20 and GN20.2a as CO[4–3] at $z = 4.05$. A concordant identification is obtained when comparing optical photometric redshifts, ACS dropout

color selection, radio–IR photometric redshifts, and optical spectroscopy from Keck.

3. Dust continuum at 3.3 mm (0.65 mm rest frame) is significantly detected for GN20, the first such measurement in a distant starburst galaxy.
4. We show that reliable radio–IR photometric redshifts (to $\Delta z \sim 0.5$) can be derived for these $z = 4.05$ galaxies using only the photometry at 24 μm , 850 μm , 3.3 mm and radio 20 cm and CE01 models. This implies that local models can be used to provide a reasonable description of the $z = 4.05$ galaxies.
5. However, evidence is also found that the dust emission from these $z \sim 4$ galaxies is somewhat colder than those of local galaxies of the same luminosities, confirming the results of P06 for lower redshift objects. In addition, the strong radio flux density of GN20.2a is taken as evidence for the presence of an AGN in this galaxy.
6. The IR to radio SEDs suggest very high IR luminosities of 2.9 and $1.6 \times 10^{13} L_{\odot}$ for GN20 and GN20.2, respectively. The CO emission lines imply molecular gas masses of 5 and $3 \times 10^{10} M_{\odot}$ for GN20 and GN20.2, respectively. For GN20 we could derive an estimate of the dynamical mass of order of $2 \times 10^{10} M_{\odot}$, implying a molecular gas fraction of order of 20% (or larger if the CO[4–3] transition is not thermalized).
7. The FIR to CO properties and SSFRs of these $z \gtrsim 4$ SMGs are similar to those of SMGs at lower redshift, $1.5 < z < 3$.
8. Radio and submillimeter stacking of *B*-band dropout galaxies, together with the SED fitting of the ACS to IRAC SEDs, is used to show that typical $z \sim 4$ star-forming galaxies have much lower SSFRs than those of SMGs at the same redshift. This suggests that the normalization of stellar mass–SFR correlation does not evolve much further in normalization beyond $z \sim 2$.
9. The GN20 and GN20.2 SMGs appear to live at the center of a strong sky overdensity of galaxies with an apparent size of 1–2 comoving Mpc, and a very significant redshift spike is seen over the full GOODS-N area, consistent with a protocluster. It is tantalizing to speculate that this overdense environment might be playing a role in triggering such extreme star formation activity (see e.g., Elbaz et al. 2007; Chapman et al. 2008).
10. Applying the newly defined radio–IR photometric redshift technique to the full sample of SMGs selected in the GOODS-N and Lockman Hole fields, we find that it provided estimates with a typical accuracy of $\Delta z/(1+z) \sim 0.15$. This is starting to approach the accuracy obtainable from optical photometric redshifts ($\Delta z/(1+z) \sim 0.06$; e.g., Brodwin et al. 2006).
11. Using this photometric redshift technique, we identify a small number of SMGs in GOODS-N where previously published optical counterparts may be in error. These SMGs lack an obvious counterpart within the SCUBA beam, these SMGs could be at quite high redshift.
12. A total of up to eight SMGs in GOODS-N (including GN20, the two counterparts of GN20.2, GN10, HDF850.1, GN13, GN28, GN04.2) are found to be consistent with having $z \gtrsim 4$. This implies a space density of similar sources around 10^{-5} Mpc^{-3} and a sizeable contribution to the cosmic SFRD at $z \sim 4$ of order of $10^{-2} M_{\odot} \text{ yr}^{-1} \text{ Mpc}^{-3}$. This is similar to that of UV-selected galaxies at the same redshifts.
13. We find that the GN20, GN20.2a, and GN20.2b galaxies and the most secure $z > 4$ SMG candidates satisfy the simple

¹⁷ <http://astronomy.sussex.ac.uk/~sjo/Hermes/>.

criterion $S_{1.4\text{GHz}} \gtrsim S_{24\mu\text{m}}$. By applying this criterion, with additional conservative constraints from optical, near-IR, and mid-IR photometry, to a sample of VLA 20 cm selected galaxies in GOODS-N, we identify three additional galaxies that appear to be reliable $z > 4$ starburst galaxy candidates. A posteriori, two of the three are found to have a detection at submillimeter/millimeter wavelengths as well.

14. Given the expected FIR fluxes of these $z > 4$ galaxies, future surveys with Herschel should allow us to characterize the properties of this population in detail.

This study is based on observations carried out with the IRAM Plateau de Bure Interferometer. IRAM is supported by INSU/CNRS (France), MPG (Germany), and IGN (Spain). We are grateful to Grant Wilson for sharing with us unpublished information from the GOODS-N AzTEC supermap. We thank Arancha Castro-Carrizo for assistance with the reduction of the IRAM Plateau de Bure Interferometer data, and Rangaraj Chary for discussions. Comments by an anonymous referee helped improving the paper. We acknowledge the use of GILDAS software (<http://www.iram.fr/IRAMFR/GILDAS>). E.D., C.M., and D.E. acknowledge support from the French ANR grant numbers ANR-07-BLAN-0228 and ANR-08-JCJC-0008. The work of D.S. was carried out at Jet Propulsion Laboratory, California Institute of Technology, under a contract with NASA. Support for this work was provided by NASA, contract number 1224666 issued by the JPL, Caltech, under NASA contract 1407.

REFERENCES

- Alexander, D. M., et al. 2003, *AJ*, **126**, 539
- Appleton, P., et al. 2004, *ApJS*, **154**, 147
- Archibald, E. N., et al. 2001, *MNRAS*, **323**, 417
- Aretxaga, I., Hughes, D. H., Chapin, E. L., Gaztañaga, E., Dunlop, J. S., & Ivison, R. J. 2003, *MNRAS*, **342**, 759
- Aretxaga, I., Hughes, D. H., & Dunlop, J. S. 2005, *MNRAS*, **358**, 1240
- Aretxaga, I., et al. 2007, *MNRAS*, **379**, 1571
- Avni, Y. 1976, *ApJ*, **210**, 642
- Blain, A. W., Chapman, S. C., Smail, I., & Ivison, R. 2004, *ApJ*, **611**, 725
- Blain, A. W., et al. 1993, *MNRAS*, **264**, 509
- Blain, A. W., et al. 2002, *Phys. Rep.*, **369**, 111
- Bolzonella, M., Miralles, J.-M., & Pelló, R. 2000, *A&A*, **363**, 476
- Bouche, N., et al. 2007, *ApJ*, **671**, 303
- Bournaud, F., et al. 2008, *A&A*, **486**, 741
- Brodwin, M., et al. 2006, *ApJ*, **651**, 791
- Calzetti, D., et al. 2000, *ApJ*, **533**, 682
- Capak, P., et al. 2008, *ApJ*, **681**, L53
- Carilli, C. L., & Yun, M. S. 1999, *ApJ*, **513**, L13
- Carilli, C. L., & Yun, M. S. 2000, *ApJ*, **530**, 618
- Chabrier, G. 2003, *ApJ*, **586**, L133
- Chapman, S. C., Blain, A. W., Ivison, R. J., & Smail, I. R. 2003, *Nature*, **422**, 695
- Chapman, S. C., Blain, A. W., Smail, I. R., & Ivison, R. J. 2005, *ApJ*, **622**, 772
- Chapman, S. C., Richards, E. A., Lewis, G. F., Wilson, G., & Barger, A. J. 2001, *ApJ*, **548**, L147
- Chapman, S. C., et al. 2008, *ApJ*, **689**, 889
- Chapman, S. C., et al. 2009, *ApJ*, **691**, 560
- Chary, R., & Elbaz, D. 2001, *ApJ*, **556**, 562
- Cimatti, A., et al. 2004, *Nature*, **430**, 184
- Cimatti, A., et al. 2008, *A&A*, **482**, 21
- Clements, D. L., et al. 2008, *MNRAS*, **387**, 247
- Condon, J. J. 1992, *ARA&A*, **30**, 575
- Daddi, E., et al. 2004a, *ApJ*, **600**, L127
- Daddi, E., et al. 2004b, *ApJ*, **617**, 746
- Daddi, E., et al. 2005a, *ApJ*, **626**, 680
- Daddi, E., et al. 2005b, *ApJ*, **631**, L13
- Daddi, E., et al. 2007a, *ApJ*, **670**, 156
- Daddi, E., et al. 2007b, *ApJ*, **670**, 173
- Daddi, E., et al. 2008, *ApJ*, **673**, L21
- Dannerbauer, H., Walter, F., & Morrison, G. 2008, *ApJ*, **673**, L127
- Dannerbauer, H., et al. 2002, *ApJ*, **573**, 473
- Dannerbauer, H., et al. 2004, *ApJ*, **606**, 664
- Dannerbauer, H., et al. 2006, *ApJ*, **637**, L5
- De Breuck, C., van Breugel, W., Minniti, D., Miley, G., Röttgering, H., Stanford, S. A., & Carilli, C. 1999, *A&A*, **352**, L51
- De Breuck, C., et al. 2004, *A&A*, **424**, 1
- Downes, D., & Solomon, P. M. 1998, *ApJ*, **507**, 615
- Dunlop, J., et al. 2004, *MNRAS*, **350**, 769
- Egami, E., et al. 2004, *ApJS*, **154**, 130
- Elbaz, D., Cesarsky, C. J., Chantal, P., Aussel, H., Franceschini, A., Fadda, D., & Chary, R. R. 2002, *A&A*, **384**, 848
- Elbaz, D., et al. 2007, *A&A*, **468**, 33
- Faber, S. M., et al. 2003, *Proc. SPIE*, **4841**, 1657
- Frazer, D. T., et al. 2006, *ApJ*, **647**, L9
- Frazer, D., et al. 2008, *ApJ*, **680**, L21
- Garrett, M. A. 2002, *A&A*, **384**, L19
- Gialalisco, M., et al. 2004a, *ApJ*, **600**, L93
- Gialalisco, M., et al. 2004b, *ApJ*, **600**, L103
- Greve, T. R., Pope, A., Scott, D., Ivison, R. J., Borys, C., Conselice, C. J., & Bertoldi, F. 2008, *MNRAS*, **389**, 1489
- Greve, T. R., et al. 2005, *MNRAS*, **359**, 1165
- Greve, T. R., et al. 2007, *MNRAS*, **382**, 48
- Griffin, M., et al. 2007, *AdSpR*, **40**, 612
- Hughes, D. H., et al. 2002, *MNRAS*, **335**, 871
- Iono, D., et al. 2006, *ApJ*, **640**, L1
- Ivison, R. J., et al. 2002, *MNRAS*, **317**, 1
- Ivison, R. J., et al. 2005, *MNRAS*, **364**, 1025
- Ivison, R. J., et al. 2007, *MNRAS*, **380**, 199
- Kennicutt, R. C., Jr. 1998, *ARA&A*, **36**, 189
- Kong, X., et al. 2006, *ApJ*, **638**, 72
- Knudsen, K. K., et al. 2008, in ASP Conf. Ser. 381, The Second Annual Spitzer Science Center Conference: Infrared Diagnostics of Galaxy Evolution, ed. R.-R. Chary, H. I. Teplitz, & K. Sheth (San Francisco, CA: ASP), **372**
- Kreysa, E., et al. 1998, *A&A*, **379**, 823
- Kriek, M., van der Wel, A., van Dokkum, P. G., Franx, M., & Illingworth, G. D. 2008, *ApJ*, **682**, 896
- Kurk, J. D., et al. 2000, *A&A*, **358**, L1
- Labbé, I., et al. 2005, *ApJ*, **624**, L81
- Le Borgne, D., et al. 2009, *A&A*, submitted, arXiv:0901.3783
- Lee, K.-S., Gialalisco, M., Gnedin, O. Y., Somerville, R. S., Ferguson, H. C., Dickinson, M., & Ouchi, M. 2006, *ApJ*, **642**, 63
- Lehmann, I., et al. 2001, *A&A*, **371**, 833
- Lin, Y.-T., Mohr, J. J., & Stanford, S. A. 2003, *ApJ*, **591**, 749
- Longhetti, M., et al. 2007, *MNRAS*, **374**, 614
- Mancini, C., et al. 2009, *A&A*, in press, arXiv:0901.3341
- Maraston, C. 2005, *MNRAS*, **362**, 799
- Maraston, C., Daddi, E., Renzini, A., Cimatti, A., Dickinson, M., Papovich, C., Pasquali, A., & Pirzkal, N. 2006, *ApJ*, **652**, 85
- McCarthy, P. J., et al. 2004, *ApJ*, **614**, L9
- Miley, G., & De Breuck, C. 2008, *A&ARv*, **15**, 67
- Miley, G. K., et al. 2004, *Nature*, **427**, 47
- Noeske, K. G., et al. 2007, *ApJ*, **660**, L43
- Paciga, G., & Scott, D. 2009, *MNRAS*, in press (arXiv:0801.0274)
- Perera, T. A., et al. 2008, *MNRAS*, **391**, 1227
- Poglitisch, A., et al. 2006, *Proc. SPIE*, **6265**, 8
- Pope, A., et al. 2005, *MNRAS*, **358**, 149
- Pope, A., et al. 2006, *MNRAS*, **370**, 1185 (P06)
- Pope, A., et al. 2008, *ApJ*, **675**, 1171
- Saracco, P., et al. 2005, *MNRAS*, **357**, L40
- Schinnerer, E., et al. 2009, *ApJL*, in press (arXiv:0810.3405)
- Scott, S. E., et al. 2002, *MNRAS*, **331**, 817
- Scoville, N., et al. 2007, *ApJS*, **172**, 38
- Solomon, P. M., & Vanden Bout, P. A. 2005, *ARA&A*, **43**, 677
- Songaila, A. 2004, *AJ*, **127**, 2598
- Spinrad, H., Dey, A., Stern, D., Dunlop, J., Peacock, J., Jimenez, R., & Windhorst, R. 1997, *ApJ*, **484**, 581
- Steidel, C. C., Adelberger, K. L., Dickinson, M., Gialalisco, M., Pettini, M., & Kellogg, M. 1998, *ApJ*, **492**, 428
- Steidel, C. C., Adelberger, K. L., Shapley, A. E., Pettini, M., Dickinson, M., & Gialalisco, M. 2003, *ApJ*, **592**, 728
- Stern, D., et al. 2005, *ApJ*, **631**, 163
- Stevens, J. A., et al. 2003, *Nature*, **425**, 264
- Tacconi, L. J., et al. 2006, *ApJ*, **640**, 228
- Tacconi, L. J., et al. 2008, *ApJ*, **680**, 246
- Takagi, T., et al. 2008, *MNRAS*, **389**, 775

- Trujillo, I., et al. 2006, *MNRAS*, **373**, L36
- Vanzella, E., et al. 2008, *A&A*, **478**, 83
- Venemans, B. P., et al. 2002, *ApJ*, **569**, L11
- Venemans, B. P., et al. 2007, *A&A*, **461**, 823
- Waddington, I., Windhorst, R. A., Cohen, S. H., Partridge, R. B., Spinrad, H., & Stern, D. 1999, *ApJ*, **526**, L77
- Wang, Z., et al. 2004, *ApJS*, **154**, 193
- Wang, W.-H., et al. 2007, *ApJ*, **670**, L89
- Wang, W.-H., et al. 2009, *ApJ*, **690**, 319
- Wiklind, T. 2003, *ApJ*, **588**, 736
- Wilson, G. W., et al. 2008, *MNRAS*, **386**, 807
- Younger, J. D., et al. 2007, *ApJ*, **671**, 1531
- Younger, J. D., et al. 2008a, *MNRAS*, **387**, 707
- Younger, J. D., et al. 2008b, *ApJ*, **688**, 59
- Yun, M. S., Reddy, N. A., & Condon, J. J. 2001, *ApJ*, **554**, 803
- Zirm, A. W., et al. 2007, *ApJ*, **656**, 66